Doctoral Dissertation

Flood Risk Assessment to Japanese Class-A Rivers using a Stochastic Precipitation Model

確率降雨モデルを用いた日本における一級河川に対する洪水リスク評価

Mizuki Shinohara

篠原　瑞生

Division of Earth and Planetary Dynamics, Department of Natural History Sciences,

Graduate School of Science, Hokkaido University

北海道大学大学院理学院自然史科学専攻

地球惑星ダイナミクス講座

2024 年 9 月

Abstract

This dissertation aims to develop a novel method to assess the flood risk for 109 class-A rivers in Japan by creating a *O*(100,000 years) precipitation data for present and future climates. A large ensemble data for precipitation were created by combining a sea-level pressure emulator developed by Kravtsov et al. (2019) with the pressure precipitation transmitter proposed by Inatsu et al. (2021). The former is based on the multi-level linear stochastic model with multiplicative noise, and the latter is based on the analogue ensemble method with a modification by the singular value decomposition. The database for Policy Decision making for Future climate change (d4PDF) was input to these models. The data were scaled up almost thirtyfold. After an appropriate bias correction to be fit with an observed quantile mapping plot, the large ensemble precipitation data that we obtained were input to a distributed rainfall-runoff model established by previous studies. It is hence demonstrated that we can evaluate the flood risk for extremely heavy precipitation with low probability for the model with parameters separately tuned for each of 109 class-A rivers in Japan. We also assessed the possible risk for climate changes based on the future climate by +2K and +4K increase in the global mean temperature. The dissertation successfully established 100,000 years of precipitation data and a 10,000-year return period of flood for a specific river, which enabled us to discuss the flood risk assessment required in the non-life insurance sector.

日本語要旨

この研究は、現在および将来気候に対する何万年分のアンサンブル降水データを作成することで、日本の 109 一級河川に対する洪水リスクを評価する新たな方法を開発することを目的とする。大規模なアンサンブル降水データは、Kravtsov ら（2019）によって開発された海面気圧エミュレーターと、Inatsu ら（2021）によって提案された気圧降水変換器を組み合わせて構築した。前者は、乗方的ノイズを持つ多層線形確率モデルに基づいており、後者は、アナログ・アンサンブルに特異値分解による修正を組み合わせた方法に基づいている。地球温暖化対策に資するアンサンブル気候予測データベース（d4PDF）をこれらのモデルに入力し、データはほぼ 30 倍に拡大された。観測されたクオンタイルマッピングプロットに適合するようにバイアス補正を行った後、得られた大規模なアンサンブル降水データを、分布型流出モデルに入力した。この結果、日本の主要 109 河川それぞれに対して極端に強い降水の洪水リスクを評価できることが示された。また、全球平均温度が+2K および+4K 上昇した未来の気候に基づいて、気候変動の可能性のあるリスクも評価した。この研究によって、特定の河川に対する 100,000 年の降水データと 10,000 年の洪水流量データを得ることで、数千年の再現期間に対応する洪水リスクを評価することに成功した。これにより、損害保険分野等で必要とされる洪水リスク評価について議論することが可能となった。

Table of contents

Abstract 1

日本語要旨 2

Chapter 1. General Introduction 5

Chapter 2. Precipitation data generation by stochastic model using large ensemble data 9

2.1. Introduction 9

2.2. Data and Method 11

2.2.1. Data 11

2.2.2. Method 12

2.3. Results 14

2.3.1. Climatology 14

2.3.2. Extreme Precipitation 16

2.3.3 Return period of extreme precipitation 17

2.3.4 Spatial and Temporal Correlation 18

2.4. Summary and Discussion 19

Chapter 3. Flood risk evaluation for Japanese class-A rivers 31

3.1. Introduction 31

3.2. Bias correction 32

3.2.1. Quantile mapping 32

3.2.2. Grid transformation 33

3.3. Runoff discharge calculations 35

3.4. Results 37

3.4.1. Annual-maximum daily precipitation 37

3.4.2. Peak discharge 39

3.5. Summary and Discussion 40

Chapter 4. General Summary 56

Acknowledgments 57

Appendix A. Sea Level Pressure emulator 58

Appendix B. Pressure-precipitation transmitter (PPT) 60

References 63

Chapter 1. General Introduction

Probabilistic risk assessment (PRA) has become increasingly important in recent years to evaluate risks associated with natural hazards such as flooding, earthquakes, volcano eruption, complex engineering systems such as an airliner and a nuclear power plant, and socio-economic or medical fields. Because risk is generally determined by the combination of hazard, exposure, and vulnerability, severe disasters rarely occur in modern societies with advanced infrastructure and highly safety standards. We then need to address events that have an extremely low probability but cause immense damage when they once occur. A valuable metric in any PRAs is the return period (RP) of hazards, which indicates the average frequency of hazardous events occurring within a specified number of years.

Floods ranked second in terms of fatalities among natural disasters, following only famine, according to world statistics in 1990s [1]. It has been reported that climate change deteriorates and will deteriorate flood frequency and damages [2]. As in the general PRA method, the RP of torrential rainfall or floods has been evaluated through analyzing the observation records and, if necessary, their statistical fitting to a parametric probability distribution. The RP is a fundamental piece of information in hard measures against flooding disasters such as determining levee height, designing dam storage capacity, constructing aqueducts, and providing detention basins. The RP is also useful when one considers soft measures. Whereas public sectors must have an initiative to soft measures such as evacuation plans, resident awareness, and dissemination of disaster information, non-life insurance is the most crucial soft measure for mitigating flood losses socio-economically. In the field of non-life insurance, the expected annual loss amount is used as the basis for calculating premiums. For events like natural disasters, where the law of large

numbers cannot be applied, relying solely on past loss data is statistically insufficient. Consequently, for statistical stability in the evaluation we need to develop probabilistic risk model. These models generate tens of thousands of hypothetical disaster events and calculate the resulting loss amounts, thereby providing a vast sample size [3]. It is worthwhile remarking that the basis for calculating non-life insurance premiums or risk amount requires the PRA with an RP that is an order of magnitude longer than that required for hard measures.

Furthermore, for not only premium calculation but also the business continuity of non-life insurance companies, it is crucial to appropriately understand and manage the existence, frequency, and risk scale of major natural disasters such as typhoons and earthquakes. This risk management method is known as Enterprise Risk Management (ERM), which is a commonly adopted risk management approach in non-life insurance companies [3] [4]. The risk amount dealt with here pertains to the loss amounts caused by extremely rare disasters, and the levels are set at 99.5% or 99.95%, corresponding to recurrence intervals of 200 to 2000 years [5] [6].

Since floods occur when rainfall exceeds the river's capacity, the PRA for flooding requires as long rainfall data-series as possible and the hydrological response to the rainfall data. If one requires a longer dataset than the observation record length in a particular river, a combination of meteorological and hydrological models is a choice other than a statistical estimation. As is well known in weather forecasting, meteorological models have advanced to resolve not only synoptic-scale disturbances but meso-scale phenomena. In the context of climate simulation, the meteorological model can be considered a type of data generative models, constrained by appropriate physical principles governing mass, momentum, and energy. On the other hand, hydrological models have recently been sophisticated, and a distributed-type model contained basin characteristics based on elevation and geological data, separation into surface

runoff and groundwater, and representation of river channels, allowing for a more reliable reproduction of water flow.

Generating a long-time rainfall dataset by meteorological models has been long performed, especially in the ensemble experiments arranged by climate model intercomparison projects (CMIPs [7]). A recent research project to develop d4PDF and its followings has been groundbreaking in generating rainfall and hydrological data spanning a period of O(1,000 years). A significant challenge encountered in such projects is the heavy computational burden associated with dynamical downscaling, which aims to enhance the resolution of meteorological data within a limited domain. The dynamical downscaling is inevitable because modern climate models with grid spacing of O(100 km) may inadequately resolve mesoscale phenomena that contribute to heavy precipitation events. Another way to generate a long timeseries of rainfall is to replace a complex physical model with a simpler statistical one. However, as discussed in Chapter 2, most previous studies have struggled to ensure temporal and spatial consistency in rainfall data even within a limited domain. An intermediate model was developed by [8], demonstrating the potential for the model to generate tempo-spatial consistent data of any desired length if we prepared a sufficient amount of reference data available. This motivates us to utilize a d4PDF's rainfall dataset as a reference of the model by [8], in order to generate enough long rainfall data to the RP required in the standards in non-life insurance field.

The goal of this dissertation is to generate 100,000-year rainfall and hydrological data capable of the PRA in the non-life insurance field. We targeted a whole Japanese territory that was covered in dynamical downscaling of d4PDF and were coped with 109 class-A Japanese rivers. Moreover, we can assess flood risk in a future climate environment. This dissertation consists of the following chapters: Chapter 2 demonstrates the application of a probabilistic

rainfall model to generate tens of thousands of years' worth of rainfall data using large ensemble datasets. It also estimates precipitation amounts for ultra-low frequency RPs. Chapter 3 applies bias corrections to the rainfall data generated in Chapter 2 and inputs it into a distributed rainfall-runoff model targeting Japan's primary river systems. This allows us to calculate extremely large flow data, ultimately estimating peak flow values for ultra-low-frequency RPs. Chapter 4 provides a summary of the research.

Chapter 2. Precipitation data generation by stochastic model using large ensemble data

2.1. Introduction

Risk assessment for a natural disaster requires not only scenario-based descriptions but also the probabilistic evaluation of disaster events [3]. The probabilistic evaluation is important for risk assessment of natural disasters. A probabilistic evaluation generally arranges three elements of risk assessment: hazard, exposure, and vulnerability. If exposure and vulnerability are specified for a target object, we must consider the remaining element of natural hazards in a stochastic sense. Natural hazards contain geophysical, meteorological, hydrological, climatological, and biological aspects. Among them, meteorological hazards frequently cause loss of lives and properties in most residential areas all over the world [9]. One used a stochastic hazard generation model that can reproduce possible extreme events. For example, the stochastic model generated thousands of tropical cyclone tracks for the probability estimate of strong wind [10] [11]. A parametric model also supports the estimation of hurricane precipitation [12] [13] [14]. The resultant output may help insurers evaluate an annual aggregated loss by a strong wind through statistical methods.

The meteorological hazards related to heavy precipitation in the midlatitudes other than tropical cyclones have hardly been modelled by a simple parametric method [15], because the heavy precipitation originated from various phenomena accompanied by complex multiscale systems. Hence, probabilistic precipitation over a limited area has been conventionally estimated by an extreme-value statistical theory using annual-maximum precipitation in historical records. This engineering approach is then applied to the design of levees and flood hazard maps published

by the government [16] [17]. Another engineering approach is the stochastic weather generator (SWG) which offers a large amount of precipitation data at a specific location [18]. Although [15] and [19] proposed a multisite SWG model that provides a timeseries of precipitation distribution with a reasonable spatial correlation among sites, the SWG approach has a reliability problem in reproducing extreme precipitation events with hundred-to-thousand year RPs [18]. On the other hand, high-speed computers enabled us to conduct a large ensemble simulation using atmospheric models. For example, the d4PDF dataset contains a set of atmospheric general circulation model output and its dynamically downscaled output both with 3,000-year length for the present climate run and 5,400-year length for a global warming run [20] [21], which made a breakthrough in the risk assessment for climate change on river flood [22] [23] [24], coastal flood [25] [26], agriculture [27] [28], snow amount [29] [30] and urban environment [31] [32] [33]. Even the d4PDF dataset is however an insufficient sample size for risk analysis in the non-life insurance field [34].

[8] developed another stochastic precipitation model with a lighter computation burden than atmospheric model runs. This model shows more reliable results in tempo-spatial distribution of precipitation than other statistical models. The model consisted of the sea level pressure (SLP) emulator developed by [35] and the pressure-precipitation transmitter (PPT), where the analog ensemble (AnEn) and singular value decomposition (SVD) are combined to obtain the precipitation data from SLP timeseries. They demonstrated that the model had a capability to provide a long timeseries of precipitation distribution in a reasonable computational time. Although [8] only showed the potential of the model based on the limited learning data of 58-year SLP and 8-year precipitation, their model based on d4PDF data is expected to provide precipitation distribution with an order of 10,000 years required by the non-life insurance field.

The purpose of this chapter is to show that a stochastic precipitation model can be applied to a large ensemble data and to provide precipitation distribution with 10,000 years. The development of SLP emulator is the idea of [35] and the combination of analog ensemble with SLP emulator is the idea of [8]. We here used the model that was already developed by [8] and the original part is what we applied it to a large ensemble dataset. The goal of this study is to estimate precipitation over a long RP in several hundred to several thousand years. Ten-thousand years are large enough to perform a PRA in the non-life insurance field. According to a rough estimate in [8], a 1,000-year RP required 50-year learning data. We assume that the 3,000-year d4PDF data is long enough to estimate the RP of the order of 10,000 years. Furthermore, this study also extends the discussion on climate change cases by the [8]'s model based on the d4PDF's global warming data. The rest of this chapter is organized as follows: Section 2.2 introduces the analysis data used here and summarizes the method in this study. The performance and the statistics of daily precipitation data from the PPT are computed with the SLP emulator in section 2.3. Section 2.4 gives a summary of this study.

2.2. Data and Method

2.2.1. Data

We used SLP and precipitation from the d4PDF datasets [20], which was a set of large ensembles with global simulations with 60-km resolution and its dynamical downscaling with 20-km resolution for the limited domain including the Japanese territory [36]. The d4PDF dataset includes the historical experiment (HPB) with 50-ensemble 1951–2010 simulation and the future climate experiments HFB2K or HFB4K, where the global-mean surface temperature increases by 2 K or 4 K relative to the preindustrial period. HFB2K (HFB4K) consists of 54 (90) ensembles

by adding detrended monthly sea surface temperatures (SSTs) in 1951–2010 to the SST warming patterns from six CMIP5 simulations[1]. Therefore, HPB, HFB2K and HFB4K experiments provided data with the length of 3,000, 3,240 and 5,400 years, respectively. The global data were used to construct the SLP emulator for the global domain; the horizontal grid size is 640 × 320 and the time interval is 6 hours. The regional data were used to obtain precipitation distribution over Japan from the SLP data; the horizontal grid size is 211×175, extracted from the original data. Though the original time interval of dynamical downscaling data is 1 hour, the data were aggregated into 6-hourly precipitation data to match the time interval of SLP data.

2.2.2. Method

The stochastic precipitation model is based on [8], consisting of the SLP emulator and PPT. A flowchart of this study is shown in Fig. 2.1. This flowchart is developed by [28] and [29] and objective analysis data is used in [28]. Following [35], we determined the model parameters of the SLP emulator by SLP anomaly data whose dimension was reduced by principal component (PC) analysis. The SLP anomaly was first created by the subtraction of daily climatological SLP

[1] The Community Climate System Model version 4 (CCSM4), the Geophysical Fluid Dynamics Laboratory Climate Model version 3 (GFDL-CM3), the Hadley Centre Global Environmental Model version 2, atmosphere-ocean (HadGEM2-AO), the Model for Interdisciplinary Research on Climate, version 5 (MIROC5), the Max Planck Institute Earth System Model, medium resolution (MPI-ESM-MR), and the Meteorological Research Institute Coupled Atmosphere-Ocean General Circulation Model version 3 (MRI-CGCM3).

from the original data. The SLP anomaly was decomposed into 1,000 PCs, which explained almost 100% of the total variance in the Northern Hemisphere. The obtained PC patterns based on d4PDF data resembled the observed one in terms of the gravest modes. We conducted the PC analysis only for the 60-year first ensemble of the HPB experiment and projected other ensemble data into the PC modes to save computation. This treatment does not likely affect the result because, whichever ensemble are selected, a sufficiently long dataset, here 60 years long, must provide a very similar vector space. We next construct a multivariate auto-regression model for the SLP anomaly from the vector data whose components consisted of 1,000 PCs. The model was formulated by three-level equations: the first level is a conventional auto-regression model to predict the time increment of PC vectors by PC vector itself; the second level is also an auto-regression model but includes the residual timeseries in the first level as an explained variable; the third level adds the residual timeseries in the second level to an explained variable. The details are described in Appendix A. The third level was also driven by a sequence of 15-day-long snippets of the residual learning data obtained in the fitting process, which was regarded as white noise. No drift was found in the SLP emulator runs in this study. The resultant vector timeseries of SLP was reconstructed and clipped to the target domain around the Japanese territory.

The PPT bridges the SLP data obtained in the SLP emulator to the precipitation distribution, which we finally obtain. We first searched for analog data from the result of SLP emulator simulation, such that three consecutive SLP snapshots are the most similar. The first guess was the precipitation distribution in d4PDF downscaling data on the analog time, following the AnEn method [8]. We next prepared the singular value decomposition (SVD). SLP anomalies and precipitation anomalies was decomposed into left and right singular vectors by SVD analysis. Based on the empirical SVD relation, we converted the SLP difference between SLP emulator

result and d4PDF result selected by AnEn to the corresponding precipitation deviation data. We added this SVD correction to the first guess as the final product. By applying SVD correction to the original rainfall data, it is expected to represent a variety of rainfall patterns beyond the original rainfall data pattern. Without SVD correction, the PPT's results are just resampled by the original precipitation data, even if various SLPs are calculated in the SLP emulator that exceeds the original pressure pattern. Therefore, it is reasonable to use SVD correction to create precipitation patterns that correspond to the SLP calculated by the SLP emulator. The details are described in Appendix B.

For the development of stochastic rainfall model, d4PDF's 60 km resolution SLP data were used to construct the SLP emulator, and 20 km resolution precipitation data were used to construct the PPT. SLP emulator's output is 6-hourly SLP pattern and PPT's output is 6-hourly precipitation.

2.3. Results

2.3.1. Climatology

Before introducing the main results, we checked the rationality of the modeled system by comparing the climatology of our model with that of the original d4PDF dataset. Both showed that the SLP climatology in boreal summer was characterized by the predominant subtropical anticyclone in the southeast of Japan (Figs. 2.2a,b) and was shifted eastward in +4K climate (Figs. 2.2c,d); [37]). The slight difference between the SLP emulator and the d4PDF dataset may stem from the use of a single ensemble member as the learning data for the SLP emulator to reduce the computational burden. The difference was larger in +4K climatology (Fig. 2.2d), because the

d4PDF simulation imposed the 6 warming patterns of SST anomaly that likely influenced the tropical and subtropical climates.

The PPT did not necessarily result in the exact match of precipitation climatology with the learning dataset of d4PDF for the random sampling from similar weather patterns in the analog process (Section 2.2). However, the result of climatology in the mean precipitation in June-July-August (JJA) months almost matched with the d4PDF's one (Figs. 2.3a,b). The total rainfall amount attained 400 mm in the 3 months in the mountainous area in Japan faced the Pacific due to orographic uplift of moisture in the windward side of the summertime Asian monsoon (Fig. 2.3b). The total rainfall amount was in contrast lower than 150 mm in northern Japan due to relatively cold and dry environment outside of the summertime monsoon influence. In addition, the PPT provided a consistent pattern of precipitation climatology with the d4PDF result (Figs. 2.3c,d); the total rainfall amount exceeded 500 mm in JJA in the windward mountainous areas of Japanese Island.

Additionally, to verify the variance of daily precipitation, the coefficient of variation, say standard deviation divided by the mean, of daily precipitation in JJA was calculated, as shown in Figs. 2.4a,b. The variance pattern is qualitatively consistent between PPT and d4PDF's HPB experiment over the domain, particularly in mountainous areas. However, the variance in the PPT results is slightly smaller than in the d4PDF. Because the precipitation variance is influenced by events, the PPT results are supposed to be underestimate extreme precipitation events. This point is addressed in Section 2.3.3, which deals with extreme precipitation events with a 100-year RP.

2.3.2. Extreme Precipitation

Figures 2.5a,b show the annual maximum daily precipitation for 100-year RP for historical simulation, defined as the top one percentile value of 10,000-year samples in our model and the top 30 value of 3,000-year samples in d4PDF datasets. The d4PDF estimated that the RP100 precipitation was ~400 mm in the area faced with the Pacific Ocean and ~150 mm in northern Japan. However, the PPT estimated that RP100 precipitation ranged 200–300 mm in the area faced with the Pacific Ocean and 100–200 mm in northern Japan. This underestimation may be due to the smoothing effect of analog ensemble method in which four 6 hourly analog data were summarized in the calculation of daily precipitation and each of those four precipitation events is independently analogous to the pressure distribution by the SLP. If an extreme precipitation event is selected as an analog, it does not necessarily mean that the other analogs for the same day are also for extreme precipitation events. The +4K simulation also showed the underestimation of RP100 precipitation by the PPT compared with the result obtained from d4PDF, where the RP100 precipitation exceeded 500 mm (Figs. 2.5c,d).

In spite of the underestimation by the PPT, the increasing rate of RP100 precipitation by the PPT almost replicated that estimated by the d4PDF (Figs. 2.6a,b). The PPT and d4PDF estimations in common showed that the RP100 increased by about 40% in Hokkaido and about 20% in other areas in Japan. It is noted that the larger increasing rate in northern Japan is consistent with the earlier study [38]. This result suggested that the PPT could be used in the creation of 10,000-year precipitation data consistent with the learning data of d4PDF if an appropriate bias correction was made.

2.3.3 Return period of extreme precipitation

Figures 2.7a,b,c,d show the annual maximum daily precipitation as a function of RP, plotted by the ranking method without any fitting formulas and determined as the inverse of the exceedance probability. The length of RP obtained by d4PDF is still limited to thousands of years whereas the PPT result can be used to estimate longer return levels.

The d4PDF's historical simulation supplied the annual maximum daily precipitation in Sapporo of ~ 80 mm for RP10, ~ 130 mm for RP100, and ~ 210 mm for RP1000 (Fig. 2.7a). In contrast with the continental climate at Sapporo, it provided ~ 200 mm for RP10, 300–350 mm for RP100, and 400–500 mm for RP1000 in the other sites in Japan (Figs. 2.7b,c,d). The d4PDF +4K simulation estimated the annual maximum daily precipitation ~ 110 mm for RP10, ~ 180 mm for RP100, and ~250 mm for RP1000 in Sapporo. The future extreme precipitation in Sapporo was less than the present extreme precipitation in Tokyo (Figs. 2.7a,b). The d4PDF +4K simulation showed 250–300 mm for RP10, 400–500 mm for RP100, and ~700 mm for RP1000 in Tokyo and Naha (Figs. 2.7b,d). This indicated that the daily precipitation of 400–500 mm occurred more frequently from RP1000 to RP100. The extreme precipitation in Fukuoka in +4K simulation was slightly moderate with 200 mm for RP10, 300 mm for RP100, and 450 mm for RP1000 (Fig. 2.7c). The d4PDF's +2K simulation showed an intermediate result between historical and +4K simulation.

As shown in RP100 precipitation (Fig. 2.5), the PPT results underestimated the annual maximum daily precipitation in any RPs (Fig. 2.7). For example, the annual maximum precipitation in historical simulation was 60 mm for RP10, 100 mm for RP100, and 140 mm for RP1000, which were 30–40% less than the d4PDF estimate. However, the increasing ratio of RP precipitation between historical and global warming simulations almost reproduced the d4PDF

estimate (Fig. 2.8). In Sapporo, the annual maximum precipitation ratio of HFB2K/HPB was 1.2 and that of HFB4K/HPB was 1.4 in RP500 or less by PPT and d4PDF (Fig. 2.8a). The d4PDF estimate rapidly decreased the ratio around RP1000 probably due to the unstable statistics for the insufficient length of sample size, but the PPT estimate gradually increased the ratio from RP500 to RP10000. The similar feature can be seen in the ratio in Tokyo (Fig. 2.8b). On the other hand, a sharp increase was seen in Naha around RP 400 in HFB4K (Fig. 2.8d). Although this may be partly related to the sampling problem, we emphasize that the extreme precipitation in Naha mostly occurred in the passage of tropical cyclones. that were not always well reproduced in the PPT method. The increasing ratio in Fukuoka was 1.2 regardless of the warming extent in d4PDF, whereas the ratio was 1.0 in HFB2K/HPB and 1.2 in HFB4K/HPB (Fig. 2.8c). The above results suggested that the PPT can reproduce the increasing rate of extreme precipitation of the d4PDF results can be used to estimate an extended RP. Taking a bias correction method [39] [40], the PPT datasets could estimate the extreme precipitation statistics with its absolute values.

2.3.4 Spatial and Temporal Correlation

The precipitation distribution by PPT corresponding to the analog based on SLP is the sum of four independent precipitation events is, so that it is not always natural for the precipitation to have a spatial correlation. We here confirm that the precipitation distribution generated by the PPT is has a reasonable spatial correlation.

The one-point spatial correlations of precipitation relative to Tokyo are shown in Fig. 2.9. The spatial correlation coefficients were higher around Tokyo, which suggested that the PPT successfully produced the spatial dependence in precipitation. The precipitation on the Sea of

Japan side has a smaller correlation coefficient, because it is mostly caused by different mechanism from the Pacific side [41]. The PPT can provide extreme precipitation with maintaining its spatial correlation whereas a stochastic weather generator cannot maintain spatial correlation.

The temporal correlation is given by the lag correlation in Fig. 2.10. In general, the observed precipitation had a short memory of less than 1 day and the d4PDF's results are similar. On the other hand, the PPT results showed a memory of about 2 days, and this trend was similar as the previous study [8], which showed no improvement even if the large number of ensemble data of d4PDF was used.

2.4. Summary and Discussion

We have used the model of the SLP emulator and the PPT and input the large ensemble climate change dataset of d4PDF to generate 10,000-year precipitation data for current and future climates. Our developed model using d4PDF data successfully reproduced climatology. The PPT underestimated the extreme precipitation probably due to the smoothing effect of summing up the analog ensembles. The PPT provided a consistent ratio of warming climate result to present climate result with the d4PDF data. Moreover, the statistics in PPT was more stable in a longer RP than 500 years. The results suggested that the PPT can reproduce the increasing rate of extreme precipitation of the d4PDF results as well as can extend the RP.

For the future risk analysis, a high-resolution model with 5 km or finer have been recently released [42]. Though such a high resolution is highly effective in capturing mesoscale rainfall phenomena, the computation burden limited the data length to few hundred years. The

dataset has an insufficient length of samples to estimate an extreme precipitation statistic such as RP1000 or longer. Our model is expected to replicate high-resolution future climate projection with a sufficient data length.

The results of this research will enable the creation of a very long-term spatiotemporal precipitation distribution dataset for the present and future climate. By combining this dataset with precipitation-runoff-inundation models, it is also possible to obtain very long-term flood discharge and inundation datasets for each water system in Japan. It is also expected to be applied to stochastic flood risk assessment considering simultaneous heavy rainfall in disaster risk modeling.

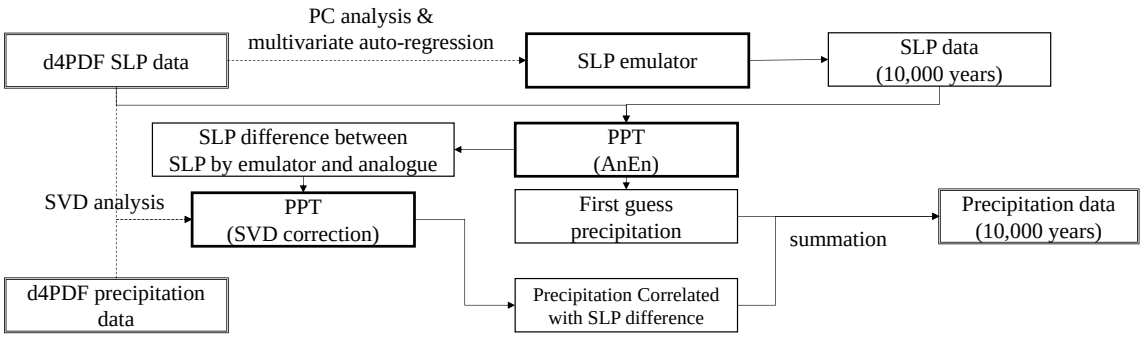

Fig. 2.1 Illustration of the usage of the SLP emulator and PPT. The input data is d4PDF SLP data (upper left) and d4PDF precipitation data (lower left) and the output data is precipitation data by PPT (lower right).

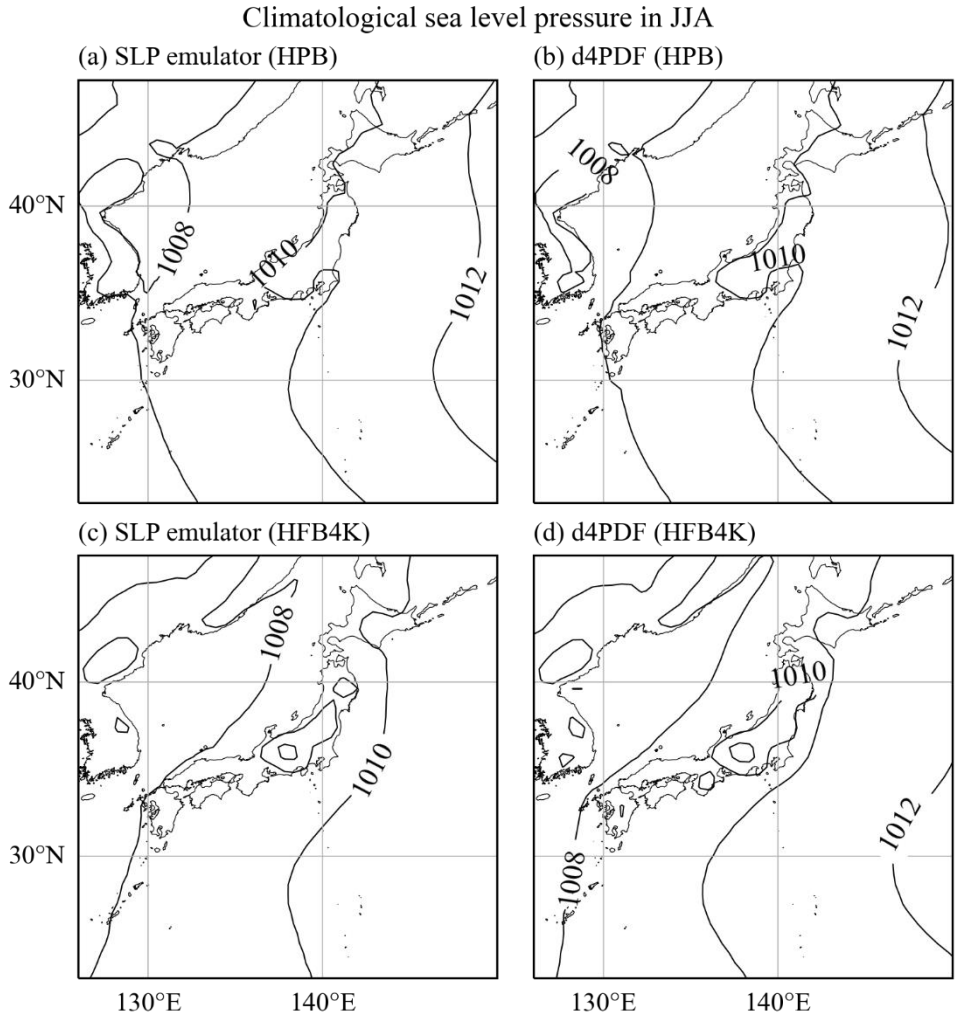

Fig. 2.2 (a,b) Climatological SLP in June-July-August (JJA) months with the contour interval being 2 hPa for (a) SLP emulator and (b) d4PDF in historical simulation HPB. (c,d) Same as (a,b) but for +4K simulation HFB4K.

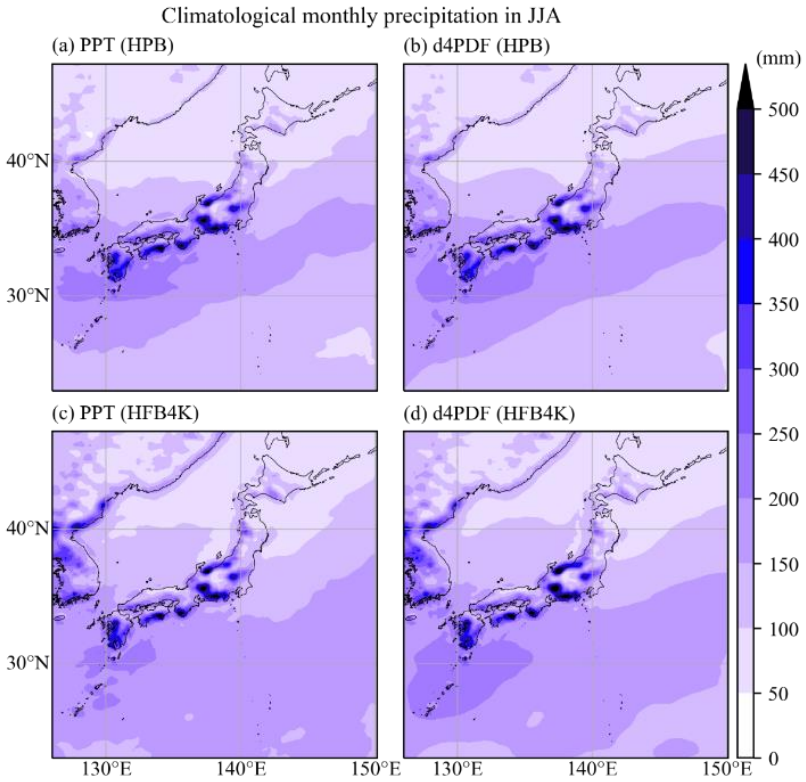

Fig. 2.3 (a,b) Climatological monthly precipitation in JJA (mm) with the color shading as per the reference in the right for (a) SLP emulator and (b) d4PDF in HPB. (c,d) Same as (a,b) but for HFB4K.

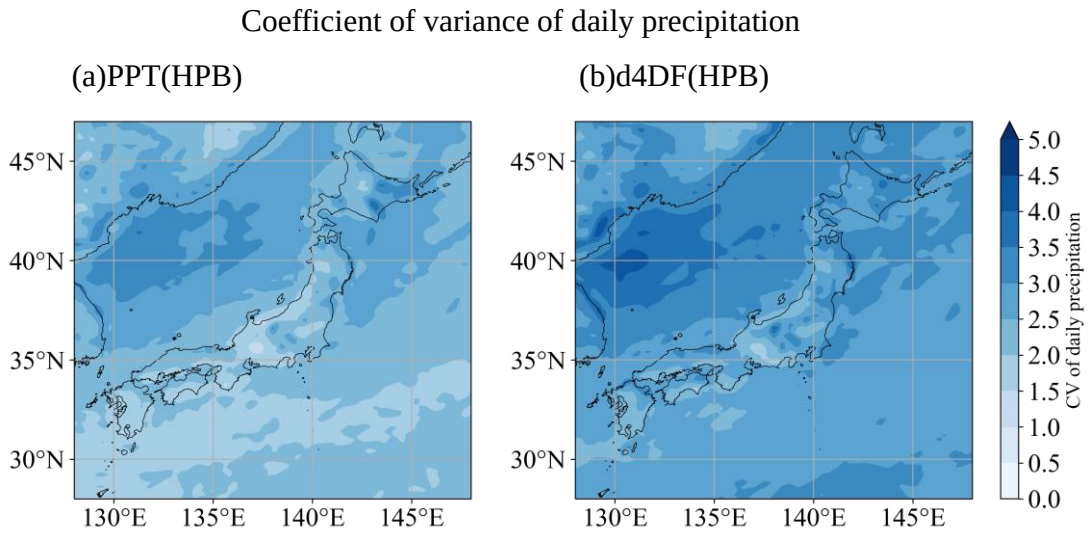

Fig. 2.4 (a,b) Coefficient of variance of daily precipitation for (a) PPT and (b) d4PDF in HPB.

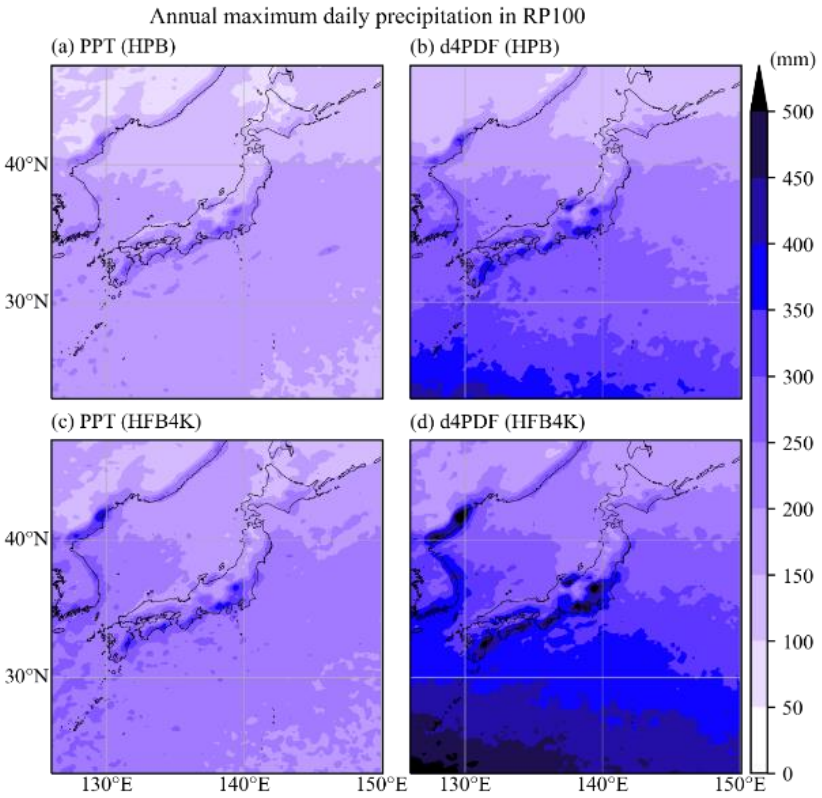

Fig. 2.5 (a,b) Annual maximum daily precipitation in the return period (RP) of 100 years for (a) PPT and (b) d4PDF in HPB. Same as (a,b), but for HFB4K.

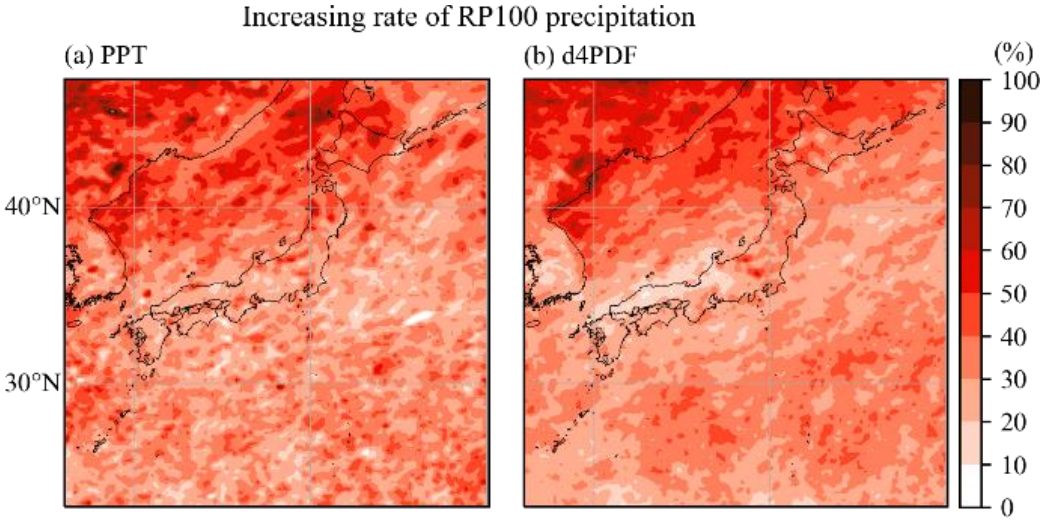

Fig. 2.6 (a,b) The increasing rate (%) of RP100 precipitation in HPB to that in HFB4K for (a) PPT and (b) d4PDF, as per the reference in the right.

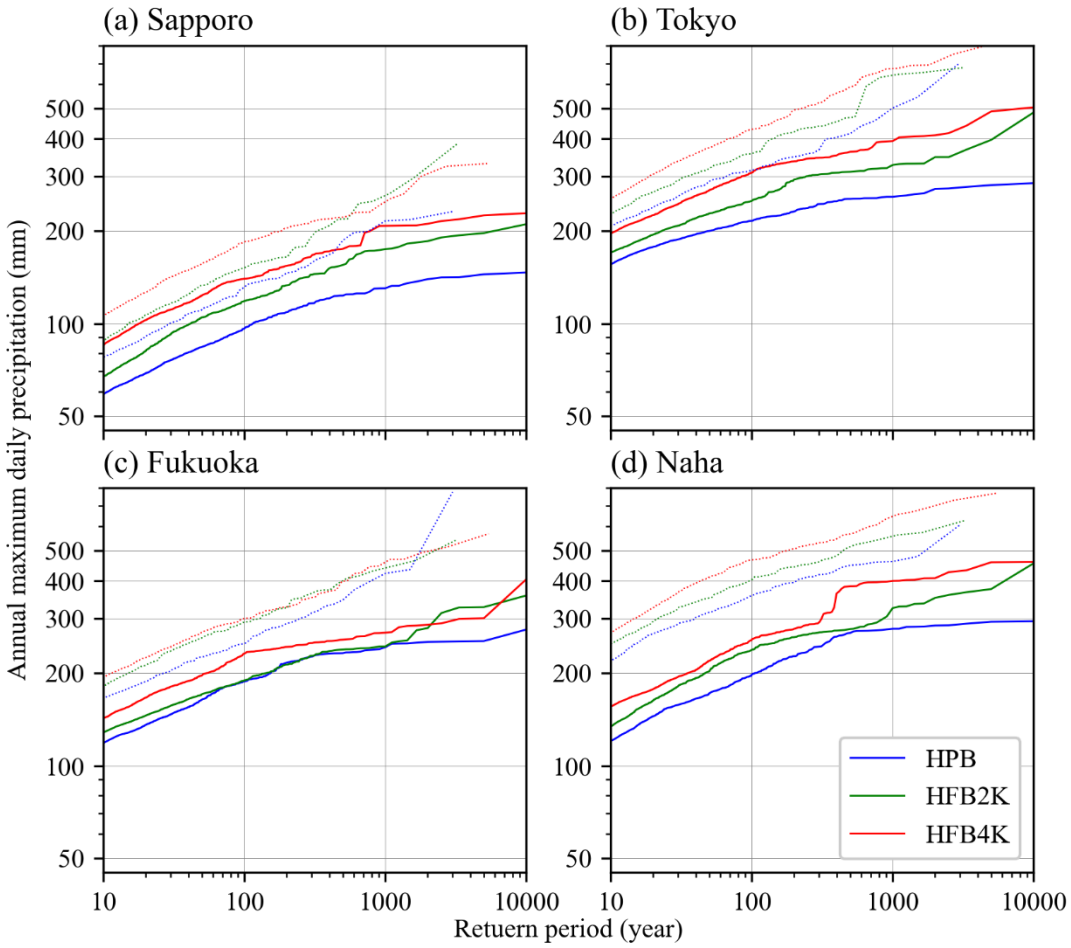

Fig. 2.7 (a,b,c,d) Annual maximum daily precipitation as a function of RP at (a) Sapporo, (b) Tokyo, (c) Fukuoka, (d) Naha for (blue) HPB, (green) HFB2K, and (red) HFB4K. Solid and dotted lines denote the results of PPT and d4PDF, respectively.

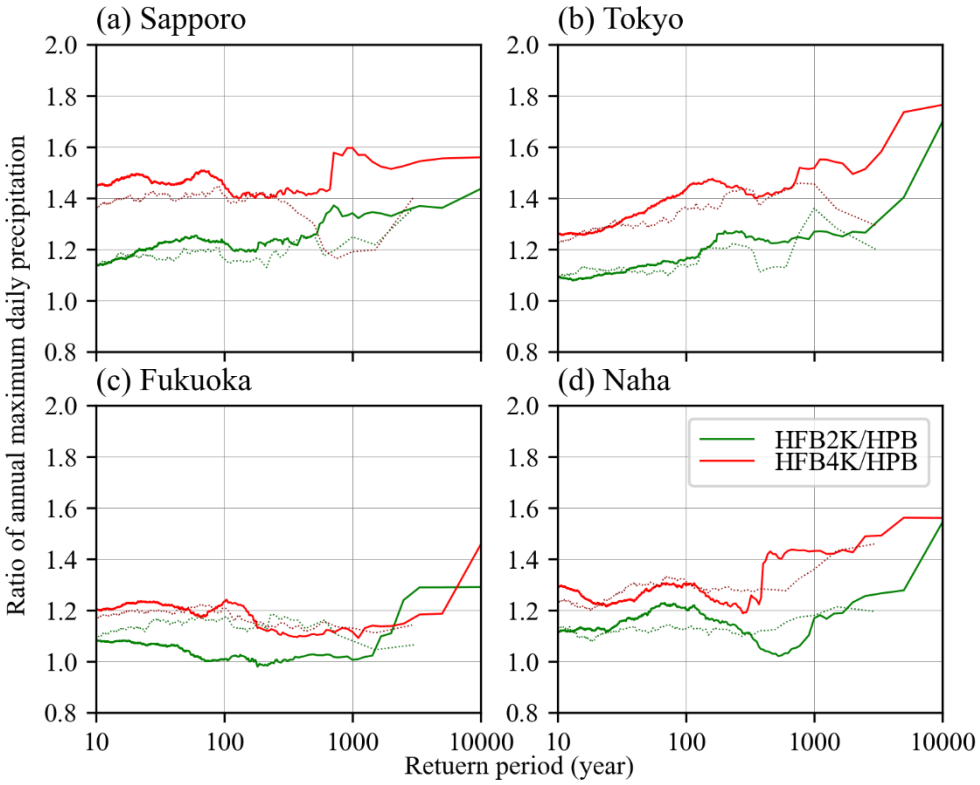

Figs.2.8 (a,b,c,d) Ratio of (green) HFB2K and (red) HFB4K to HPB of annual maximum daily precipitation as a function of RP at (a) Sapporo, (b) Tokyo, (c) Fukuoka, and (d) Naha. Solid and dotted lines denote the results of PPT and d4PDF, respectively.

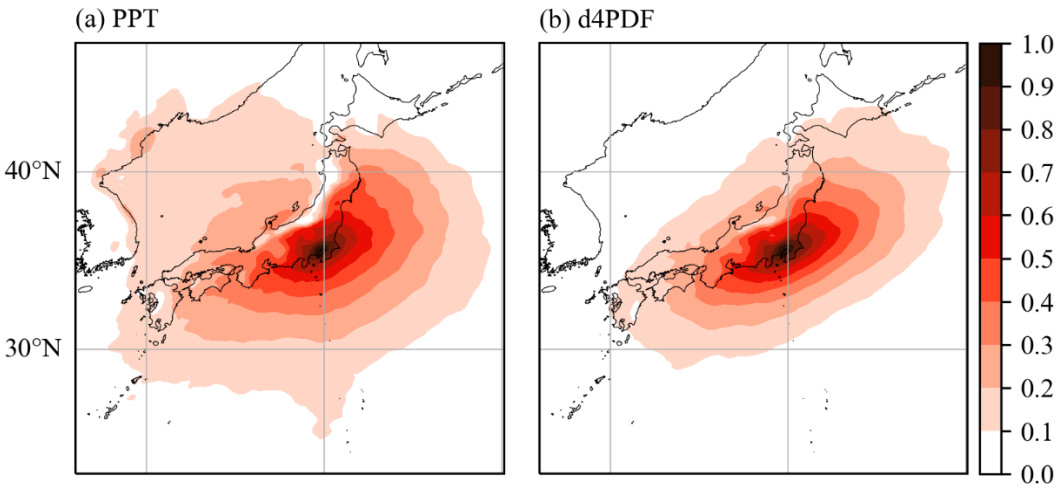

Fig. 2.9 (a,b) Correlation coefficients of daily precipitation relative to Tokyo. HFB4K for (a) PPT and (b) d4PDF.

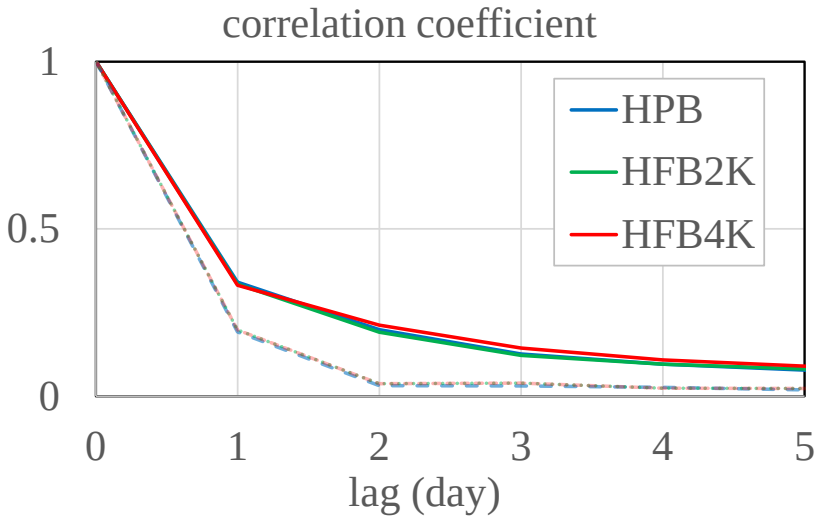

Fig. 2.10 The lag autocorrelation of daily precipitation of the (blue) HPB, (green) HFB2K, and (red) HFB4K. Solid and dotted lines denote the results of PPT and d4PDF, respectively.

Chapter 3. Flood risk evaluation for Japanese class-A rivers

3.1. Introduction

In recent years, there has been a series of severe damages caused by large-scale floods. We can raise Japanese examples of persistent heavy rainfall in western Japan in July 2018 and torrential rainfall in eastern Japan associated with Typhoon Hagibis in 2019. These events enhanced interests and concerns of public and private sectors about flood risk assessment in Japan. However, as stated in General Introduction, PRA applied to flooding risk requires a large amount of rainfall and hydrological data. Recently, the release of d4PDF with *O*(1000 year) length seems to be a clue to resolving this issue. In fact, many attempts have been done for flood risk assessment by d4PDF in Japan, mostly by inputting the downscaled rainfall data to a hydrological model.

[22] analyzed the future changes in flood discharge by this manner for three rivers in Japan, Arakawa River through Tokyo metropolitan area, Shonai River in Yamagata Prefecture, and Yodo River in Shiga to Osaka Prefectures. [43] analyzed the future changes in flood risk throughout Japan by inputting the runoff generation data of d4PDF into a river flood model CaMa-Flood. [44] constructed a distributed rain-runoff model for all class-A river systems in Japan, including the river flow adjustment by dam controls. They calculated the annual maximum peak flow for the rivers and analyzed the future changes in river flow by inputting annual maximum precipitation events obtained from the downscaled precipitation data of d4PDF. Despite the recent advancement of PRA for flooding in Japan shown above, since the number of ensembles in d4PDF is limited to a few thousand years at most, the data length is still insufficient to meet the demand of the non-life insurance sector. Although [45] discussed the simultaneous occurrence probability of floods in multiple rivers, increasing the number of ensembles remains a challenge for the future.

This chapter aims to generate a large amount of river flow ensemble data, which enables us to discuss flood risk corresponding to the ultra-low frequent events for 109 class-A rivers in Japan (Table 3.1, Fig. 3.1). Specifically, a large amount of flow data is generated by inputting the rainfall data generated by the probabilistic rainfall model constructed in Chapter 2 into the distributed rain-runoff model. The rest of this chapter is organized as follows: Section 3.2 describes the bias correction made to the rainfall data computed in Chapter 2; Section 3.3 provides an overview of the runoff model used to compute the flows; Section 3.4 provides the results of the computed flows and a discussion of the results.

3.2. Bias correction

3.2.1. Quantile mapping

This section describes bias correction of rainfall data. Bias correction is generally made to mitigate systematic bias in the model by comparing model output with observation data. Among various methods that have been proposed [46], we chose quantile mapping, one of the most general methods in bias correction for rainfall. In the quantile mapping, a correction factor was determined by the ratio of model data to observed data for the same RP (Fig. 3.2). It is worthwhile remarked that this study coped with several tens of thousands of years of model rainfall data. The number of years is much larger than observation records of rainfall with its length spanning at most several decades. A correction factor for the RP exceeding the limitation of observation was estimated by an extrapolation of a fitting function in quantile mapping. It should be cared that this treatment possibly brought the large uncertainty particularly for extremely long RPs beyond the observation limitation (Fig. 3.3a).

In this study, the simulated rainfall data were first divided into 50-year segments, and

an RP curve for annual-maximum daily precipitation is created for each segment, as described in [47]. We then computed the median of annual-maximum daily precipitation based on all RP curves. The ratio to the observed precipitation in the quantile map is identified as the bias correction factor. The bias correction can be made by multiplying simulated rainfall in each segment by the correction factor. This method provides the way to mitigate the problem in the bias correction for the number of simulated data with longer length than observation record (Fig. 3.3b).

3.2.2. Grid transformation

The simulated rainfall data were arranged by 0.2-degree mesh covering land areas over Japan. However, bias correction should be performed for a different grid system of the watershed mesh data provided by the Ministry of Land, Infrastructure, Transport and Tourism (MLIT). In the watershed mesh data, the central points of the watershed mesh and inland water classification mesh included in each mesh describing watersheds belonging to each tertiary mesh 1/10 subdivision (100-m mesh) are counted, and then the area of the mesh included in each water system A_s is measured, where s = 1, 2, ..., 109 is water system classification. The rainfall for each water system category, P_s, is the weighting average over the model grid-points inside of the category as follows,

$$P_s = \sum_m p_m A_m \Big/ \sum_m A_m, \tag{3.1}$$

where p_m is rainfall at a model grid-point m. The daily rainfall for each water system category was obtained by the sum of four 6-hour rainfalls in a particular day, and then the annual-maximum daily rainfall can be extracted.

The annual-maximum daily rainfall for each water system category is used to generate a RP curve. The annual-maximum daily rainfall data are divided into groups with the same data length of 50 years and sorted in the descending order within each group. The median value was calculated to create a RP curve of daily rainfall for each water system category, and the RP was estimated as

$$\mathrm{RP} = \frac{N+1}{i}. \tag{3.2}$$

Here $N = 50$ is the number of years in each group, and $i = 1, 2, 3, ..., N$ denotes the descending rank.

Next, the observed rainfall data are processed. The monthly maximum daily rainfall from January 1970 to December 2019 at stations nationwide is obtained, and the simple average is taken for each water system category to which it belongs. From this, the annual-maximum daily rainfall is extracted and sorted in the descending order, and the RP is given using the Weibull formula in Eq. (3.2), where N is the number of years in which at least one monthly maximum daily rainfall was obtained. This enabled us to create a reproduction period curve for daily rainfall for each water system category.

Finally, correction factors are determined as the ratio of the median value of simulation rainfall to the observed rainfall for the same RP. The corrected data are created by multiplying the correction factor with the original data for each group. The corrected annual-maximum daily rainfall for all groups is then sorted in the descending order, and the RP is given again using Eq. (3.2). An RP curve of corrected daily rainfall for each water system and inland water category was obtained in this manner.

3.3. Runoff discharge calculations

This section overviews the distributed rainfall-runoff model that we used. It was the kinematic wave model 1K-DHM, developed by the Department of Social Infrastructure Engineering, Graduate School of Engineering, Kyoto University [48]. This model divides the watershed into grid cells with a latitude-longitude grid of 30 seconds (approximately 1 km) and calculates flood flow from upstream to downstream by specifying flow directions between cells (Figs. 3.4, 3.5). Rainwater flow on each cell is composed of slope elements and channel elements. In the slope elements, the outflow to the channel is calculated and is then transferred as lateral inflow to the channel elements. The river flow at the downstream end of the channel element becomes the flow for that cell. In the slope elements, the following continuity equation (3.3) and momentum equation (3.4) are solved to calculate the outflow (Fig. 3.6).

$$\frac{\partial h}{\partial t} + \frac{\partial q}{\partial x} = r, \text{where} \tag{3.3}$$

$$q = \begin{cases} d_c k_c \left(\frac{h}{d_c}\right)^{\beta} i & (0 \le h \le d_c) \\ d_c k_c i + (h - d_c) k_a i & (d_c \le h \le d_a). \\ \frac{\sqrt{i}}{n_s}(h - d_a)^m + (h - d_c) k_a i + d_c k_c i & (d_a \le h) \end{cases} \tag{3.4}$$

Here, r represents rainfall intensity, h denotes the water depth of overland flow, d_c corresponds to the water depth associated with the matrix portion of the top soil layer, d_a represents the water depth related to the large void portion within the top soil layer, k_c signifies the saturated hydraulic conductivity of the matrix portion, and β is a parameter indicating the attenuation due to the degree of unsaturation of the hydraulic conductivity. The unsaturated hydraulic conductivity of the matrix portion is denoted by $k_c \left(\frac{h}{d_c}\right)^{\beta}$. Additionally, using β, we established a relationship

between the saturated hydraulic conductivity of the large void portion k_a and that of the matrix portion k_c as $\mathrm{k_a} = \beta \mathrm{k_c}$. n_s represents Manning's roughness coefficient, and i denotes the slope gradient. The value of $m = 3/5$ can be determined from Manning's formula.

For the channel element, the following continuity and kinematic equations are solved to calculate the river flow Q (Fig. 3.6).

$$\frac{\partial A}{\partial t} + \frac{\partial Q}{\partial x} = q, \text{and} \tag{3.5}$$

$$Q = \frac{\sqrt{i}}{B^{2/3} n_r} A^m, \tag{3.6}$$

where A is the cross-sectional area of the channel, n_r is the roughness coefficient of the channel, and B is the channel width. The six model parameters to be identified are n_s, d_c, d_a, k_c, β, and n_r.

In watersheds where dams exist, the following dam model is also applied in the cell where the dam is located to calculate the discharge $Q'(t)$ from the cell.

$$Q'(t) = \begin{cases} I(t) \ \left(I(t) < Q_f\right) \\ Q_f \ \left(I(t) \geq Q_f \text{ and } S_r < S_{\mathrm{SL}} - S_{\mathrm{NL}}\right)' \end{cases} \tag{3.7}$$

where $I(t)$ is the inflow at time t, S_{SL} is the effective storage volume, S_{NL} is the flood stage storage capacity, and Q_f is the starting flood control flow rate. When the inflow exceeds the flood control start flow, the discharge is limited to the flood control start flow Q_f. When the storage volume exceeds the flood storage capacity, the inflow is again released. The above discharge method is called the constant volume discharge method. Despite that it is not the unique way, the constant discharge method was adopted here as used in many dams in Japan as a reasonable approximation. In this study, rainfall data generated in Chapter 2 and the differing

temporal and spatial resolutions inherent to 1kDHM were adjusted accordingly. The temporal resolution of 1kDHM is 1 hour with a spatial resolution of 1 km. In contrast, the output from PPT, used as input, has a temporal resolution of 6 hours and a spatial resolution of 20 km. Therefore, for temporal resolution, the average hourly precipitation from PPT's output, calculated over 6 hours, was input into 1kDHM. For spatial resolution, in 1kDHM, rainfall data for each computational grid (1 km) were input using the data from the nearest grid [49].

3.4. Results

3.4.1. Annual-maximum daily precipitation

As described before, the rainfall-runoff model experiment will be performed for annual-maximum daily precipitation after bias correction. The bias correction effectively worked even in a massive amount of precipitation data that we obtained in Chapter 2. We now showed an example in the case of Arakawa River (Fig. 3.7). Following the procedure introduced in Section 3.2, we prepared 2,000 segments of 50-year precipitation data and drew 2,000 RP curves based on the annual-maximum daily precipitations. The bias correction factor was determined by the ratio of the median of simulated curves to the observation curve for each rank from 1 to 50. We multiply simulated precipitation data in each 50-year segment by the bias correction factor. It is certain that the RP curve of bias-corrected data was reasonably fit with the observation curve in the 50-year RP. This practically provided the RP curve in the part exceeding 50 years. We made sure the simulated data was well fit with the observed data for all 109 class-A rivers (not shown). The bias correction was also made for the precipitation data not only of historical experiment but of 2K and 4K experiments by the same bias correction factor, which is an important preprocessing for the risk increase due to climate change based on the PRA in flooding. Before demonstrating the

precipitation and hydrological change due to climate change, we will check that the precipitation data generated by our probabilistic model was consistent with the previous study [38]. We followed the classification of Japanese territory of northern/southern Hokkaido, western/eastern Tohoku, Kanto, Hokuriku, Chubu, Kinki, Kii, San'in, Setouchi, western Chugoku, southern Shikoku, and northwestern/southeastern Kyushu. The ratio of 2K experiment to historical experiment (Fig. 3.8) almost ranged between 1.1 and 1.2. The results are in a general agreement with [38] with a slight overestimation in central to western Honshu Island and slight underestimation in Hokkaido and Shikoku.

The annual-maximum daily precipitation was generally large in a warm climate. For example, the 100-year RP is about 150 mm in Ishikari River, Hokkaido (Fig. 3.9a) and is about 300 mm in Arakawa, Yodo, and Chikugo Rivers (Figs. 3.9b,c,d). Our probabilistic approach provided the RP of 1000 years and longer. It is just our finding that the 10,000-year RP exceeds 200 mm in Ishikari River, around 500 mm in Arakawa and Yodo Rivers, and about 400 mm in Chikugo River. The increase in global temperature generally enhanced the heavy precipitation hazard and the RP curves showed larger annual-maximum daily precipitations. For example, Ishikari River has 10,000-year RP at approximately 400 mm in 4K experiment, comparable to that in Chikugo River under the historical experiment (Figs. 3.9a,d). The Chikugo River moreover showed it at approximately 700 mm in 4K experiment (Fig. 3.9d). Compared with these two rivers, the increase is not so prominent in Arakawa and Yodo River (Figs. 3.9b,c). It is ~ 600 mm in Arakawa River (Fig. 3.9b) and ~ 500 mm in Yodo River (Fig. 3.9c). The 2K experiment results is almost an intermediate between historical and 4K experiments.

These characteristics can be representative of Hokkaido, Kanto, Kinki and Kyushu regions, which can be seen in the increasing ratio of precipitation amount for the 100-year RP in

109 class-A rivers (Fig. 3.10). Most of class-A rivers in Hokkaido exhibited the ratio ~1.2 for 2K experiment and 1.4-1.5 for 4K experiment. The ratio is almost comparable in most of class-A rivers in Tohoku, Kanto and Chubu districts, but the ratio for 4K experiment seemed slightly less than in Hokkaido. In contrast, the ratio is ~1.0 to 1.1 for 2K experiment and ~1.2 to 1.3 for 4K experiment in western Japan.

3.4.2. Peak discharge

Inputting the annual-maximum daily precipitation data obtained from our probabilistic model, the hydrological model output the river discharge for historical and 4K experiment. Figure 3.11 summarizes the runoff model calculations in the flow amount as a function of the reproduction period in Ishikari, Arakawa, Yodo, and Chikugo Rivers. Discharge calculations are computed at a reference point in each river (Ishikari-Ohashi, Ishikari, Hokkaido for Ishikari River, Iwabuchi in Akabane, Tokyo for Arakawa, Hirakata, Osaka for Yodo River and Arase, Ukiha, Fukuoka for Chikugo River), and peak discharge is obtained from the maximum value of the time series discharge.

The peak discharge for 1,000-year RP under the current climate is ~ 35,000 m^3/s in Ishikari River, ~ 6,000 m^3/s in Arakawa River, ~ 12,000 m^3/s in Yodo River, and ~ 7,000 m^3/s in Chikugo River, which depends on the river channel cross section. In all the rivers, climate change with the global temperature increase by 4K augments the flow rate for any RPs. For example, the 1,000-year RP of peak discharge increased to ~52,000 m^3/s in Ishikari River, ~7,500 m^3/s in Arakawa River, 13,000 m^3/s in Yodo River, and 9,000 m^3/s in Chikugo River.

Despite that the increasing rate depends on rivers, the results are consistent with the RP of rainfall input to the hydrological model. Generating extremely long rainfall data with the length

of 10,000 years enabled us to obtain the peak flow values for highly rare RPs exceeding 1,000 years. Figure 3.12 shows the increase rate of peak discharge in the comparison between historical and 4K experiments. The increase ratio ranged between 1.1 to 1.4, consistent with the literature [38]. In terms of the increase rate by RP for each river, the Ishikari River shows an approximately 1.4-fold increase from the 100-year RP to 2,000 years, with a slight decrease in the increase rate for periods exceeding 5,000 years. The Arakawa River exhibits about a 1.6-fold increase at the 100-year RP, but this value generally decreases to around 1.2-fold for periods exceeding 200 years. As for the Yodo and Chikugo Rivers, no significant tendency for the RP is observed, with increase rates ranging from approximately 1.1 to 1.3 across all RPs.

3.5. Summary and Discussion

In this Chapter, we eventually achieved the purpose of this dissertation to generate 100,000-year rainfall and hydrological data capable of the PRA in the non-life insurance field by the established distributed rainfall-runoff model forced by precipitation data provided by our probabilistic rainfall model. We successfully listed up the precipitation hazard as 100-year, 1000-year, and 10,000-year RPs for all class-A rivers in Japan (e.g. Fig. 3.10), and this information should be the basis of the hydrological estimation. The peak discharge amount, a kind of metrics to evaluate potential flooding, was estimated by the hydrological model. The annual-maximum daily precipitation produced by our probabilistic model enabled us to estimate the RP at 1,000-year and longer. As shown in the Ishikari, Arakawa, Yodo, and Chikugo Rivers, the climate change with global-mean temperature increases by 4K increased the peak discharge by 1.1 to 1.4 times (Fig. 3.11). It was also found that the increase ratio depends on the RP in some case (Fig. 3.12).

It should be noted that there are uncertainties associated with calculating bias correction

factors. The method used in this study involves correcting rainfall data between observed data from the past 50 years and simulated data. However, discussing appropriate correction factors for extreme RPs beyond the observed period remains challenging. Additionally, various bias correction methods have been proposed [46], leading to differences in the results. These uncertainties may impact the runoff calculation results.

The quantile mapping used in this study largely depends on the distribution characteristics of the data. For example, it is significantly influenced by the uncertainty of outliers and low-frequency values [46]. To address these issues and discuss the uncertainty of the model, it is necessary to compare the results of multiple bias correction methods and evaluate the robustness of the results in future.

It also should be noted that, as described in Section 3.3, the resolution of the rainfall data generated by the probabilistic rainfall model is 6 hours and 20 km. The spatiotemporal resolution of rainfall data in flood runoff calculations largely depends on the catchment area and runoff timescale of the river in question. In general, the finer the resolution becomes, the better the accuracy is. As stated in [50] [51] when estimating river flow in Japan, it is desirable for the spatial resolution to be less than 20 km. Therefore, the calculation results of PPT have a somewhat coarse resolution, which can introduce uncertainty into the runoff calculation results.

To address this issue, usage of the finer resolution rainfall data would be a solution. Currently, in the Japan Meteorological Agency [52] large-scale ensemble rainfall data with a resolution of 5 km are being prepared and published. Although such data may not cover a large number of sample years, they excel in spatial and temporal resolution and have the potential to resolve the uncertainty in this study.

Table 3.1 List of class-A rivers in Japan.

#	River name	District	Catchment area (km^2)	Reference Point
1	Teshio River	Hokkaido	5,590	Pompira
2	Shokotsu River	Hokkaido	1,240	Kamishokotsu
3	Yubetsu River	Hokkaido	1,480	Kaisei
4	Tokoro River	Hokkaido	1,930	Kitami
5	Abashiri River	Hokkaido	1,380	Bihoro
6	Rumoi River	Hokkaido	270	Owada
7	Ishikari River	Hokkaido	14,330	Ishikariohashi
8	Shiribetsu River	Hokkaido	1,640	Nakoma
9	Shiribeshi-Toshibetsu River	Hokkaido	720	Imakane
10	Mukawa River	Hokkaido	1,270	Mukawa
11	Saru River	Hokkaido	1,350	Biratori
12	Tokachi River	Hokkaido	9,010	Moiwa
13	Kushiro River	Hokkaido	2,510	Shibecha
14	Iwaki River	Tohoku	2,540	Goshogawara
15	Takase River	Tohoku	867	Uwano（Ogawarako）
16	Mabuchi River	Tohoku	2050	Ohashi
17	Kitakami River	Tohoku	10,150	Goshodamu（Kosenji）
18	Naruse River	Tohoku	1,133	Sambongi
19	Natori River	Tohoku	939	Natoribashi
20	Abukuma River	Tohoku	5,390	Iwanuma
21	Yoneshiro River	Tohoku	4,100	Futatsui
22	Omono River	Tohoku	4,710	Tsubakikawa
23	Koyoshi River	Tohoku	1,190	Todoroki
24	Mogami River	Tohoku	7,040	Ryoubashi
25	Akagawa River	Tohoku	857	Kumaide
26	Kuji River	Kanto	1,490	Yamagata
27	Naka River	Kanto	3,270	Noguchi
28	Tone River	Kanto	16,840	Yattajima
29	Arakawa River	Kanto	2,940	Yorii
30	Tama River	Kanto	1,240	Ishihara

31	Tsurumi River	Kanto	235	Kamenoko（Sueyoshibashi）
32	Sagami River	Kanto	1,680	Sagamiohashi
33	Fuji River	Chubu	3,990	Kitamatsuno
34	Arakawa River	Chubu	1,150	Hanadate
35	Agano River	Chubu	7,710	Maoroshi
36	Shinano River	Chubu	11,900	Ojiya
37	Seki River	Chubu	1,140	Takata
38	Hime River	Chubu	722	Yamamoto
39	Kurobe River	Chubu	677	Unazukidamu（Aimoto）
40	Joganji River	Chubu	368	Kameiwa
41	Jinzu River	Chubu	2,720	Jinzuohashi
42	Sho River	Chubu	1,180	Ogami
43	Oyabe River	Chubu	682	Tsuzawa
44	Tedori River	Chubu	809	Tsurugi
45	Kakehashi River	Chubu	271	Komatsuohashi
46	Kano River	Chubu	852	Ohito
47	Abe River	Chubu	567	Tegoshi
48	Oi River	Chubu	1,280	Kanza
49	Kiku River	Chubu	158	Kamo（Kuniyasu）
50	Tenryu River	Chubu	5,090	Kajima
51	Toyo River	Chubu	724	Ishida
52	Yahagi River	Chubu	1,830	Iwazu
53	Shonai River	Chubu	1,010	Biwajima
54	Kiso River	Chubu	5,275	Inuyama
55	Suzuka River	Kinki	323	Takaoka
56	Kumozu River	Kinki	550	Kumozubashi
57	Kushida River	Kinki	436	Ryogun（Ryogumbashi）
58	Miya River	Kinki	920	Iwade
59	Yura River	Kinki	1,882	Ayabe
60	Yodo River	Kinki	8,240	Hirakata
61	Yamato River	Kinki	1,070	Kashiwara
62	Maruyama River	Kinki	1,300	Tachino
63	Kako River	Kinki	1,730	Oshima
64	Ibo River	Kinki	810	Tatsuno

65	Kino River	Kinki	1,660	Funato
66	Shingu River	Kinki	2,360	Oga
67	Kuzuryu River	Kinki	2,930	Nakatsuno(Fuseda）
68	Kita River	Kinki	210.2	Takatsuka
69	Chiyo River	Chugoku	1,190	Gyotoku
70	Tenjin River	Chugoku	490	Koda
71	Hino River	Chugoku	870	Kuzumo
72	Hii River	Chugoku	2,540	Kamishima
73	Gono River	Chugoku	3,900	Kawamoto（Gotsu）
74	Takatsu River	Chugoku	1,090	Takatsuno
75	Yoshii River	Chugoku	2,110	Tsuyama（Iwato）
76	Asahi River	Chugoku	1,810	Shimomaki
77	Takahashi River	Chugoku	2,670	Sakazu（Funao）
78	Ashida River	Chugoku	870	Yamate
79	Ota River	Chugoku	1,710	Nakano（Kumura）
80	Oze River	Chugoku	340	Yasakadamu(Ryogokubashi)
81	Saba River	Chugoku	423	Shimbashi
82	Yoshino River	Shikoku	3,750	Iwazu
83	Naka River	Shikoku	874	Furusho
84	Doki River	Shikoku	140	Haraikawabashi
85	Shigenobu River	Shikoku	445	Deai
86	Hiji River	Shikoku	1,210	Ozu
87	Monobe River	Shikoku	508	Fukabuchi
88	Niyodo River	Shikoku	1,560	Ino
89	Watari River	Shikoku	2,186	Gudo
90	Onga River	Kyushu	1,026	Hinodebashi
91	Yamakuni River	Kyushu	540	Shimotobaru
92	Chikugo River	Kyushu	2,860	Arase
93	Yabe River	Kyushu	620	Funagoya
94	Matsuura River	Kyushu	341	Mutabe（Matsurabashi）
95	Rokkaku River	Kyushu	341	Mizonokami（Suminoebashi）
96	Kase River	Kyushu	368	Ikemori（Kanjimbashi）
97	Honmyo River	Kyushu	249	Urayama
98	Kikuchi River	Kyushu	996	Tamana

99	Shira River	Kyushu	480	Myokembashi（Yotsugibashi）
100	Midori River	Kyushu	1,213	Jonan
101	Kuma River	Kyushu	1,880	Hitoyoshi（Yokoishi）
102	Oita River	Kyushu	650	Funaiohashi
103	Ono River	Kyushu	1,465	Shiratakibashi
104	Banjo River	Kyushu	464	Banjoohashi
105	Gokase River	Kyushu	1,820	Miwa
106	Komaru River	Kyushu	474	Omaruohashi（Takajo）
107	Oyodo River	Kyushu	2,230	Kashiwada
108	Sendai River	Kyushu	1,573	Kamimasaki（Sendai）
109	Kimotsuki River	Kyushu	485	Matase

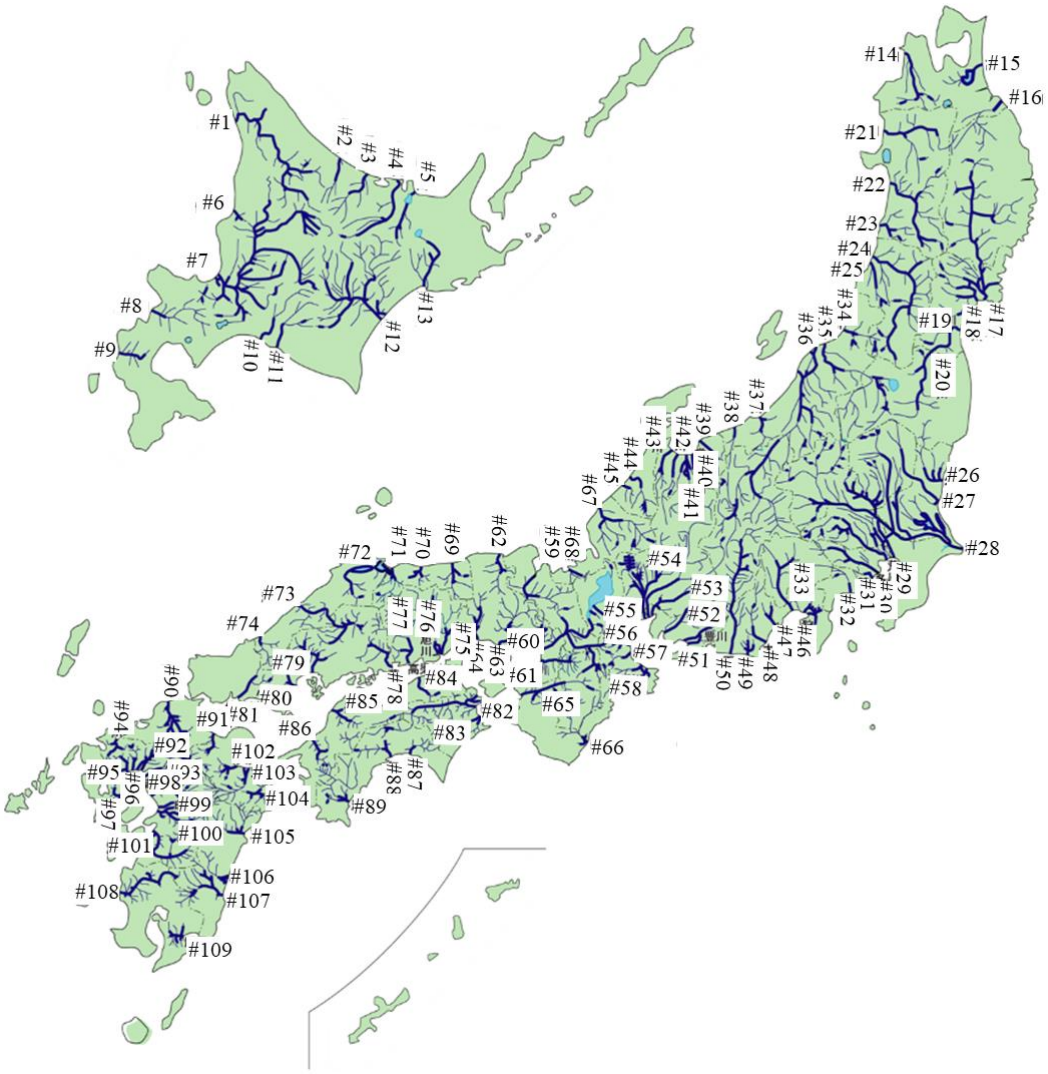

Fig. 3.1 Geographical map of Japan with emphasizing 109 class-A rivers (See Table 3.1 for the number) with thin lines indicating tributary. We modified the website at Ministry of Land, Infrastructure, Transport and Tourism of [53].

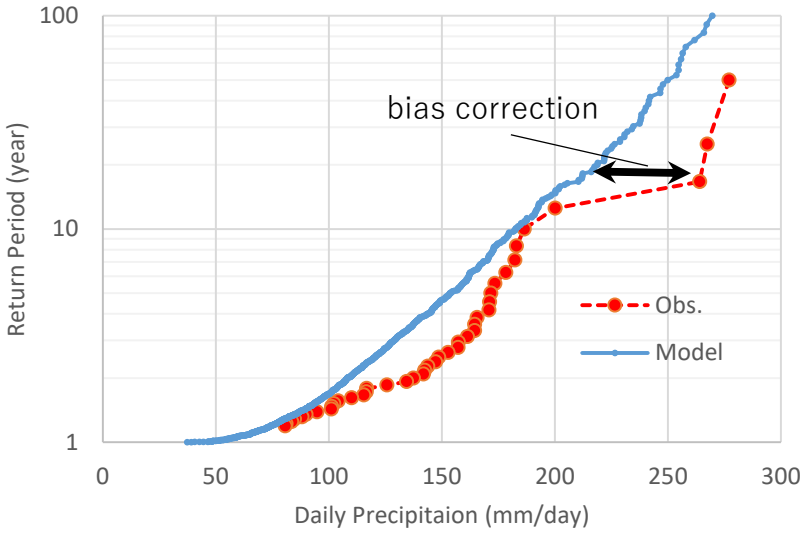

Fig. 3.2 Illustration of quantile mapping bias correction method applied to rainfall data.

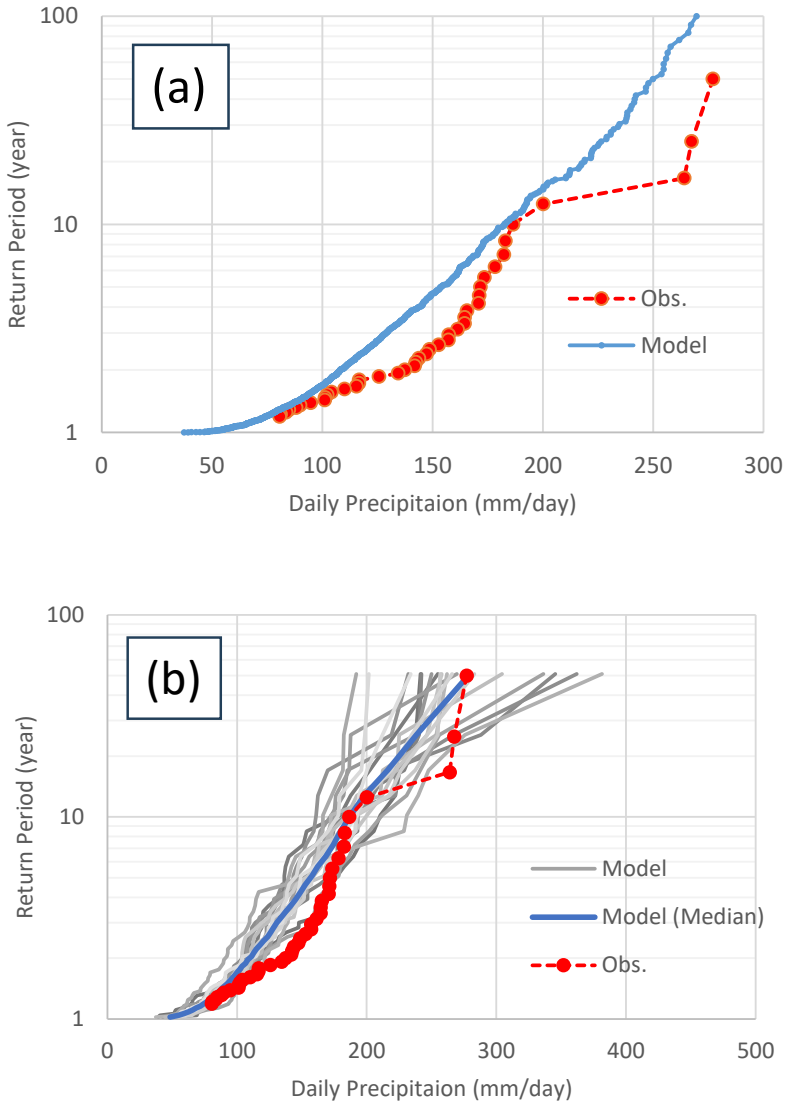

Fig. 3.3 (a; blue line) The quantile mapping with all simulated rainfall data making a single RP curve versus (red dot) the observation. (b; gray lines) The quantile mapping with a set of segments for simulated rainfall data making multiple RP curves versus (red dots) the observation. Blue line denotes the median of the curves.

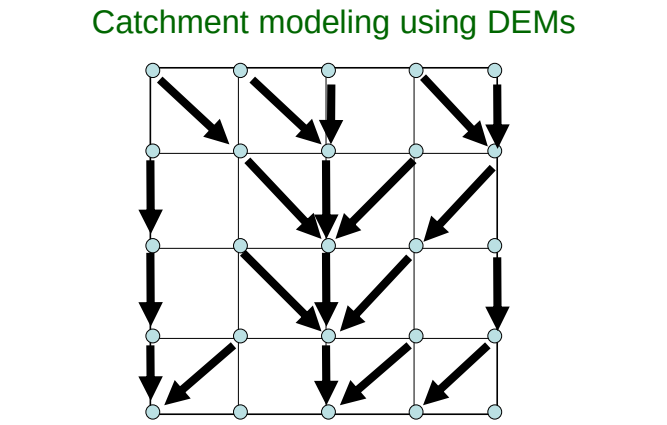

Fig. 3.4 Illustration of a downgradient direction in the model cell in a catchment area. Materials received from Dr. Tomohiro Tanaka, Kyoto University.

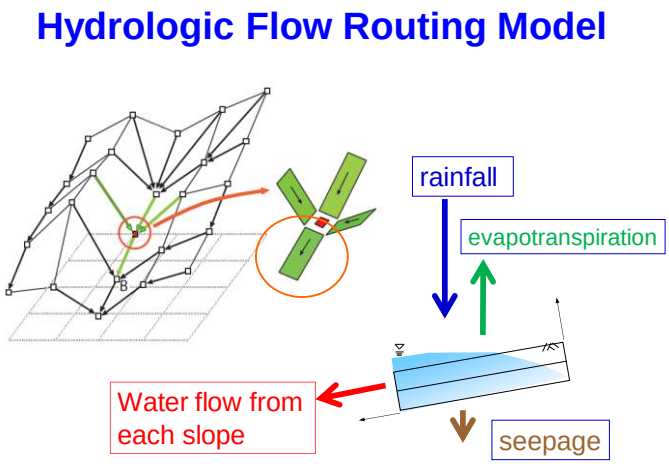

Fig. 3.5 (Left) Illustration of hydrologic flow routing model. (Right bottom) Illustration for the water flow dynamics and mass balance in a cell shown in the center schematics. Materials received from Dr. Tomohiro Tanaka, Kyoto University.

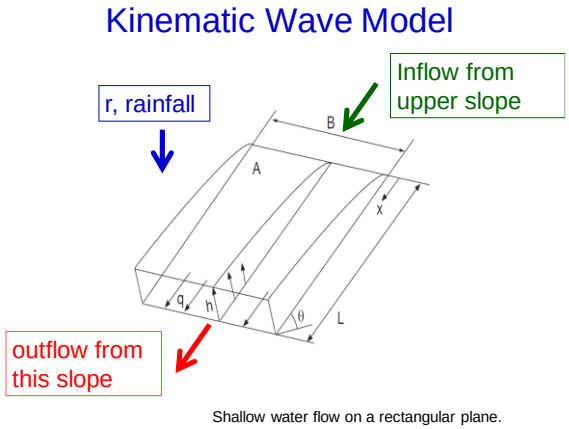

Fig. 3.6 A conceptual diagram of kinematic wave model in a slope element. Materials received from Dr. Tomohiro Tanaka, Kyoto University.

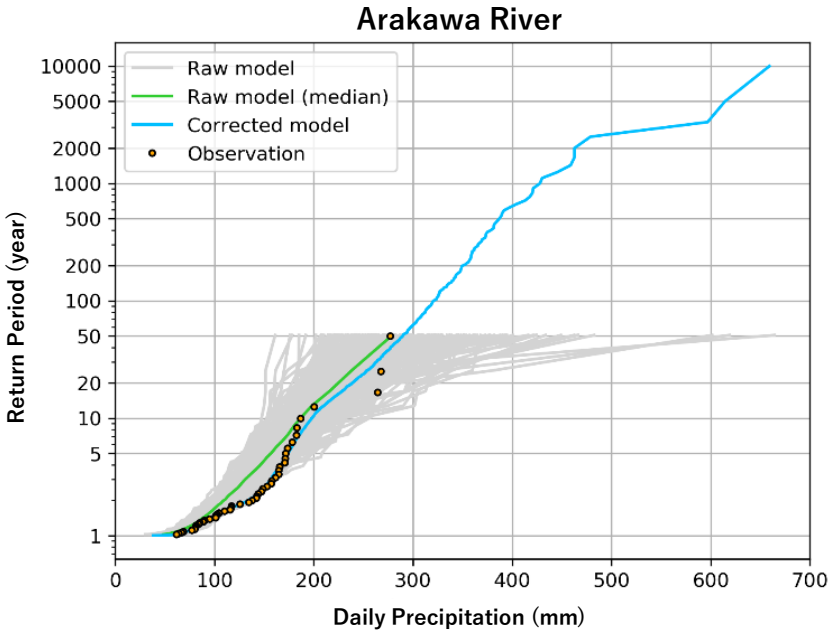

Fig. 3.7 RP curves as a function of annual-maximum daily precipitation (mm) for Arakawa River. Green line denotes the median of (gray lines) a bundle of 50-year segment data obtained by our probabilistic model. Blue line denotes the bias corrected data by (dots) observed precipitation data.

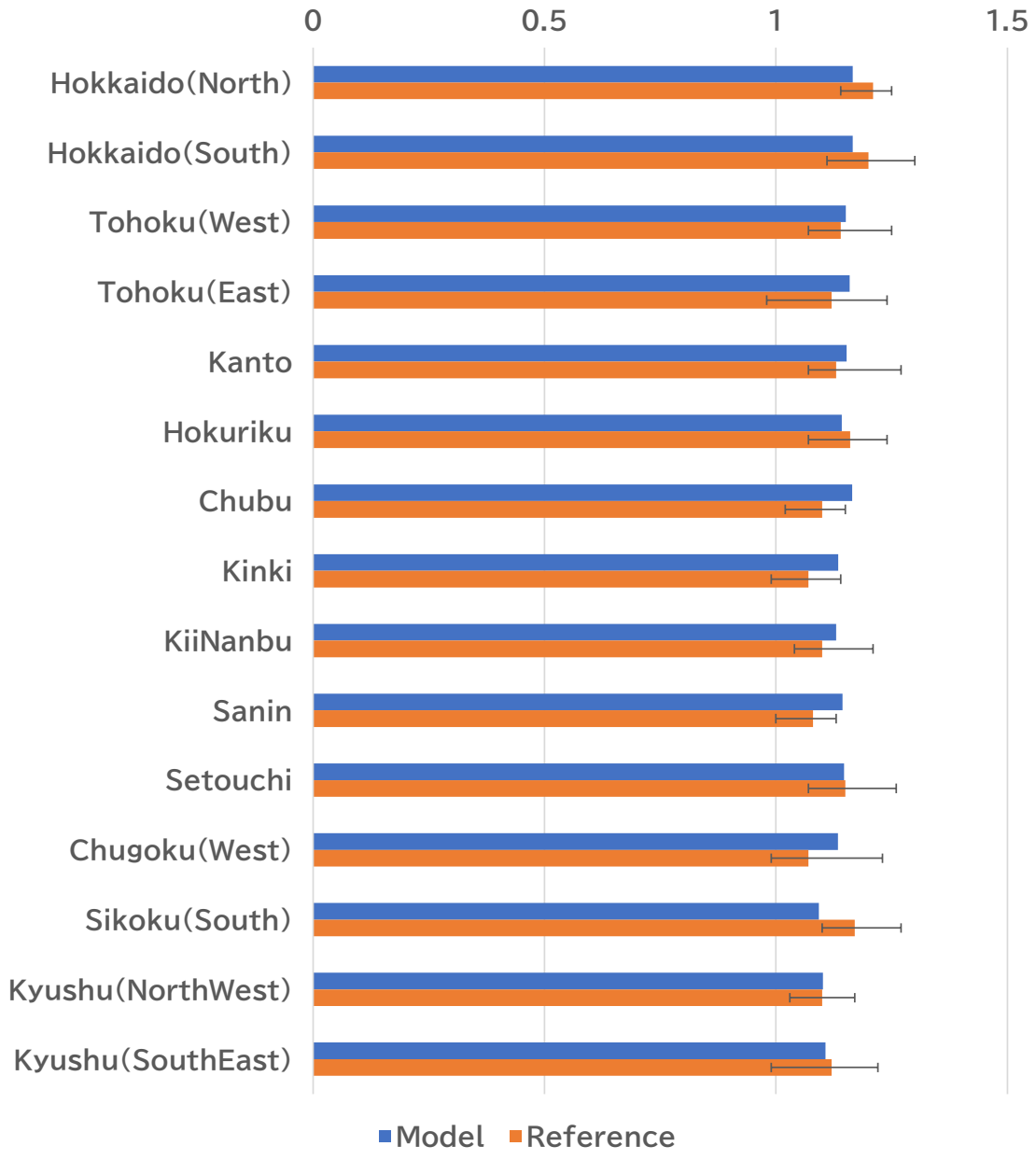

Fig. 3.8 Comparison of rainfall increase rate for 2 K temperature increase scenario with reference [38].

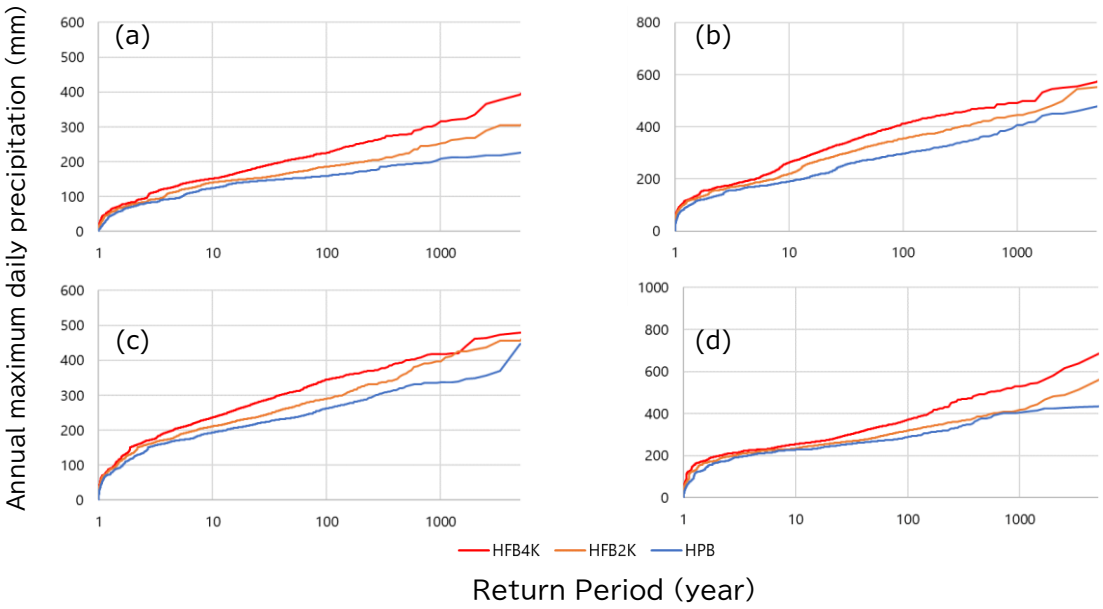

Fig. 3.9 Annual maximum daily precipitation (mm) as a function of RP (year) for (a) Ishikari, (b) Arakawa, (c) Yodo, and (d) Chikugo Rivers. Blue, yellow, and red lines respectively denote the results for historical, 2K, and 4K experiments.

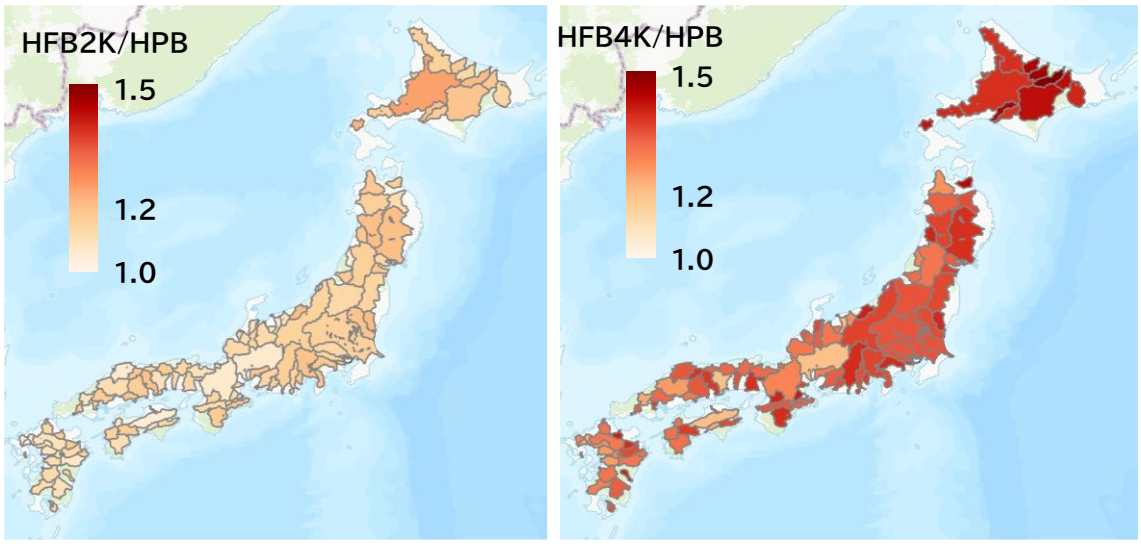

Fig. 3.10 The increase rate of 100-year RP rainfall for 109 Class-A rivers in Japan. Left is 2K experiment and right is 4K relative to historical experiment.

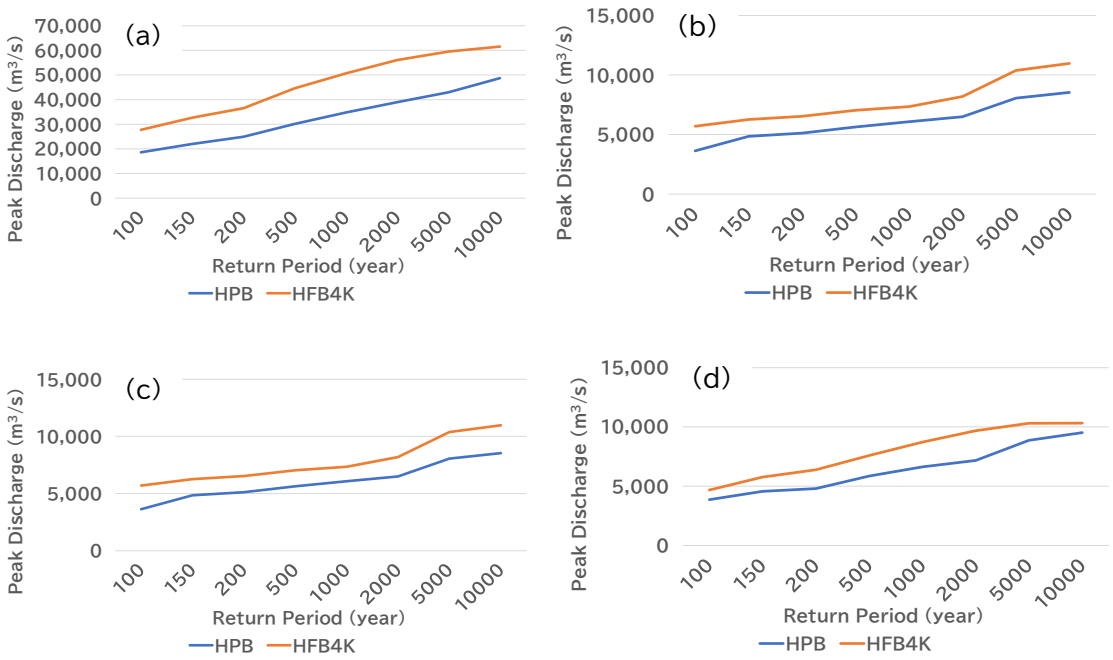

Fig. 3.11 Peak discharge (m^3/s) as a function of RP (year) for (blue) historical and (orange) 4K experiment in (a) Ishikari, (b) Arakawa, (c) Yodo, and (d) Chikugo Rivers.

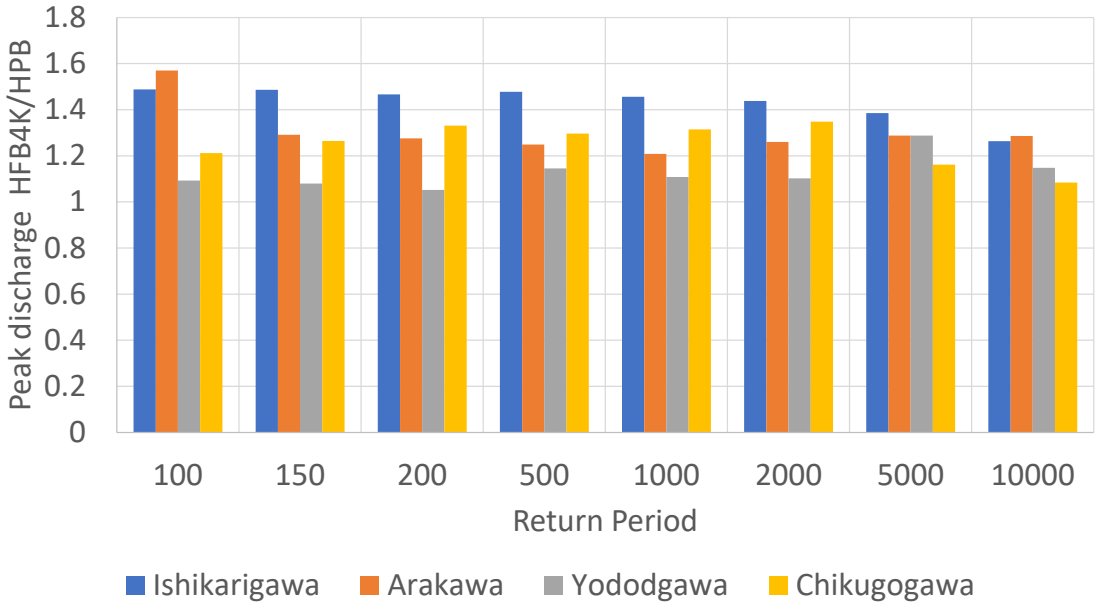

Fig. 3.12 The increase rate of peak discharge between historical and 4K experiments for (blue) Ishikari, (orange) Arakawa, (gray) Yodo, and (yellow) Chikugo Rivers.

Chapter 4. General Summary

The goal of this dissertation was to obtain precipitation and river flow with extremely low probability from a large ensemble data as an output of a sequence of use of three models: SLP emulator, pressure-precipitation transmitter, and distributed rainfall-runoff model. An appropriate bias correction was made before inputting precipitation data into the latest model.

In Chapter 2, a probabilistic meteorological model was constructed following [8] with a reference dataset of the large-scale ensemble dataset d4PDF. We here demonstrated the ability to generate tens of thousands of years of rainfall data. The statistical analysis of the generated rainfall data enabled us to estimate precipitation for highly rare events ranging from hundreds to thousands of years in the RP. Moreover, based on datasets of global warming experiments, an extremely large ensemble rainfall data was generated in the future climate conditions.

In Chapter 3, the generated rainfall data from Chapter 2 were bias-corrected and input into a distributed rainfall-runoff model targeting the primary water systems nationwide to calculate flow rates, resulting in the computation of extremely large flow rate data. Similar to the rainfall data, the statistical analysis enabled us to estimate peak flow rates for highly rare events.

Using the rainfall and river flow data generated in this study, it becomes possible to calculate flood risks corresponding to highly rare events by, for example, calculating the damage cost due to floods. The results can be utilized in various aspects of natural disaster risk management in the industry, such as estimating the required capital size for huge disasters for insurance companies and estimating economic losses for general business companies considering climate change.

Acknowledgments

I would like to express my gratitude thanks to Prof. Masaru Inatsu, who is the chief referee of my doctoral thesis, for supporting this study and suggesting valuable comments and discussions. I also deeply thank all associate referees, Prof. Shoshiro Minobe, Dr. Yoshinori Sasaki, Dr. Yousuke Sato, and Dr. Tomohiro Tanaka. I also thank Dr. Sho Kawazoe and Dr. Takumi Honda for giving me insightful comments to this work. I thank Ms. Kao Mizushima for co-operation about precipitation model, and Dr. Daiki Ajima and Mr. Daisuke Kato for giving me insightful comments about run-off model and bias correction. I thank Ms. Atsuko Kobayashi and Choko Maeda for supporting office procedures and thank the other laboratory members for giving me great time. Finally, I would like to express our deepest gratitude to Tokio dR Co., Ltd. for their unwavering support and valuable contributions to this research.

Appendix A. Sea Level Pressure emulator

This section describes the construction of the SLP emulator. The SLP emulator is built following the methodologies outlined in [8] and [35]. As the first step in constructing the SLP emulator, the empirical orthogonal function (EOF) patterns of daily SLP anomalies from d4PDF were computed. The SLP anomaly data can be accurately reconstructed using the 1000 leading modes of the EOF decomposition, which explain 99.9% of the variance in the SLP anomalies.

Next, for the time series scores of each decomposed mode, a three-level vector autoregression model is constructed for each month, described as

$d\mathbf{s} = \mathbf{A}^{(0)}\mathbf{s} + \mathbf{e}^{(1)}$,	(A1)
$d\mathbf{e}^{(1)} = \mathbf{A}^{(1)}[\mathbf{e}^{(1)}\ \mathbf{s}] + \mathbf{e}^{(2)}$, and	(A2)
$d\mathbf{e}^{(2)} = \mathbf{A}^{(2)}\left[\mathbf{e}^{(2)}\ \mathbf{e}^{(1)}\ \mathbf{s}\right] + \mathbf{e}^{(3)}$,	(A3)

where $\mathbf{s}$ is a 1000-dimensional vector that stores the time series scores, and $\mathbf{e}^{(1)}$, $\mathbf{e}^{(2)}$, and $\mathbf{e}^{(3)}$ represent the residuals of the first, second, and third levels of the VAR model, respectively. The left side of the equations represents the temporal change in the corresponding variables. This three-level VAR model estimates the propagator $\mathbf{A}^{(0)}$, $\mathbf{A}^{(1)}$, and $\mathbf{A}^{(2)}$ from the time series of the 1000 modes of the principal components.

After estimating the propagator $\mathbf{A}^{(0)}$, a 1000×1000 matrix, the residual $\mathbf{e}^{(1)}$ was obtained from the data. At the second level, the predictor variables are the time series scores $\mathbf{s}$ and the first-level residual $\mathbf{e}^{(1)}$, making the size of the propagation term $\mathbf{A}^{(1)}$ 2000×1000. Similarly, the residual $\mathbf{e}^{(2)}$ can be obtained from the learning data using Eq. (2). At the third level, the predictor variables

are the time series scores and residuals from the first and second levels. The propagation matrix $\mathbf{A}^{(2)}$ of size 3000×1000 was estimated. Finally, we complete the three-level VAR model.

Using the above procedure, the residual time series $\mathbf{e}^{(1)}$, $\mathbf{e}^{(2)}$, and $\mathbf{e}^{(3)}$ for each month were obtained from the regression equations based on the time series scores. The residual time series $\mathbf{e}^{(3)}$ for the entire learning data period is saved as a noise library and used for calculation of SLP.

Appendix B. Pressure-precipitation transmitter (PPT)

This section describes the construction of the PPT. The PPT is built following the methodologies outlined in [35]. First, a daily SLP time series was obtained by the simulation by the SLP emulator (Section 2.2 and Appendix A). The output forms the vector in the space spanned by 1000 EOF modes, and then we created the SLP data by a spatial reconstruction. It is noted that the original output with a daily interval were temporally interpolated to 6-h time intervals.

Next, the SVD analysis truncated at mode K was conducted independently for each month to identify a spatial pattern that exhibits a high correlation between precipitation and three consecutive SLP snapshots. A set of three temporally adjacent SLP anomalies p'_a was decomposed into the left singular vectors $\{\boldsymbol{u_1}, \boldsymbol{u_2}, \dots, \boldsymbol{u_K}\}$ normalized as

$$\boldsymbol{r_a}(t) = \sum_{k=1}^{K} a_k(t)\, \boldsymbol{u_k}, \tag{B1}$$

where

$$\boldsymbol{r_a}(t) = \begin{pmatrix} p'_{a,1}(t-6\text{h}) \\ \vdots \\ p'_{a,I}(t-6\text{h}) \\ p'_{a,1}(t) \\ \vdots \\ p'_{a,I}(t) \\ p'_{a,1}(t+6\text{h}) \\ \vdots \\ p'_{a,I}(t+6\text{h}) \end{pmatrix}, \tag{B2}$$

just lumping the three consecutive SLP snapshots together, and I is the total number of grid-points in a single SLP snapshot. The precipitation anomaly, P'_a, was also decomposed into the right singular vectors $\{\boldsymbol{v_1}, \boldsymbol{v_2}, \dots, \boldsymbol{v_K}\}$ normalized as

$$\boldsymbol{R_a}(t) = \sum_{k=1}^{K} b_k(t)\, \boldsymbol{v_k^T}, \tag{B3}$$

where

$$\boldsymbol{R_a}(t) = \begin{pmatrix} P'_{a,1}(t) \\ \vdots \\ P'_{a,J}(t) \end{pmatrix}, \tag{B4}$$

and J is the total number of grid-points in a single precipitation snapshot.

In the third step, by searching the SLP data in the d4PDF, we identify the N's closest neighbors at t_1, t_2, …, t_N to the SLP emulator output around a particular time t_0, by calculating the total square difference over the target area. The first guess of precipitation at t_0 is the geometric mean of the learning precipitation data, $P_a(\boldsymbol{\xi}, t)$, over the set of times as,

$$\ln \widetilde{P_f}(\boldsymbol{\xi}, t_0) = \frac{1}{N} \sum_{n=1}^{N} \ln P_a(\boldsymbol{\xi}, t_n), \tag{B5}$$

whereas the corresponding SLP is the arithmetic mean of the three adjacent SLP snapshots as

$$\begin{pmatrix} \widetilde{p_f}(\boldsymbol{\xi}, t_0 - 6\mathrm{h}) \\ \widetilde{p_f}(\boldsymbol{\xi}, t_0) \\ \widetilde{p_f}(\boldsymbol{\xi}, t_0 + 6\mathrm{h}) \end{pmatrix} = \frac{1}{N} \sum_{n=1}^{N} \begin{pmatrix} p_a(\boldsymbol{\xi}, t_n - 6\mathrm{h}) \\ p_a(\boldsymbol{\xi}, t_n) \\ p_a(\boldsymbol{\xi}, t_n + 6\mathrm{h}) \end{pmatrix}. \tag{B6}$$

The discrepancy between the original SLP emulator output and the aforementioned first guess is discretized and forms the $3I$-dimensional vector of

$$\boldsymbol{r'_f}(t_0) = \begin{pmatrix} p_{f,1}(t_0 - 6\mathrm{h}) - \widetilde{p_{f,1}}(t_0 - 6\mathrm{h}) \\ \vdots \\ p_{f,I}(t_0 - 6\mathrm{h}) - \widetilde{p_{f,I}}(t_0 - 6\mathrm{h}) \\ p_{f,1}(t_0) - \widetilde{p_{f,1}}(t_0) \\ \vdots \\ p_{f,I}(t_0) - \widetilde{p_{f,I}}(t_0) \\ p_{f,1}(t_0 + 6\mathrm{h}) - \widetilde{p_{f,1}}(t_0 + 6\mathrm{h}) \\ \vdots \\ p_{f,I}(t_0 + 6\mathrm{h}) - \widetilde{p_{f,I}}(t_0 + 6\mathrm{h}) \end{pmatrix}. \tag{B7}$$

The orthonormality of the left SVD vectors allows us to find the coefficients corresponding to $\boldsymbol{r'_f}(t)$ as

$$a'_k = \boldsymbol{r'_f}(t_0)\, \boldsymbol{u_k^T}. \tag{B8}$$

The precipitation anomaly correlated with the difference between original SLP emulator output and the first guess is hence given as

$$\boldsymbol{R'_f}(t_0) = \sum_{k=1}^{K} a'_k\, \boldsymbol{v_k^T} \sqrt{\int b_k^2(\tau)\, d\tau \Big/ \int a_k^2(\tau)\, d\tau}, \tag{B9}$$

which can be reconstructed as $P'_f(\boldsymbol{\xi}, t_0)$.

The PPT ultimately offers the precipitation estimate corresponding to the SLP emulator output, $\widetilde{p_f}(\boldsymbol{\xi}, t_0)$, as the sum of the AnEn's first guess and the SVD correction: The final product is then written as

$$\widehat{P_f}(\boldsymbol{\xi}, t_0) = \widetilde{P_f}(\boldsymbol{\xi}, t_0) + P'_f(\boldsymbol{\xi}, t_0). \tag{B10}$$

References

[1] International Federation of Red Cross and Red Crescent Societies, “World Disasters Report,” 2004.

[2] The Intergovernmental Panel on Climate Change, “Sixth Assessment Report, Climate Change 2021: The Physical Science Basis,” 2021.

[3] K. Mitchell-Wallace, M. Jones, J. Hillier, and M. Foote, Natural catastrophe risk management and modelling: a practitioner's guide, John Wiley & Sons, 2017.

[4] S. Matsuo, “Underwriting and Quantitative Portfolio Management of Catastrophic Risks in Non-Life Insurance,” Journal of Insurance Science, Volume 2013 Issue 620 Pages 620_97-620_116, 2013.

[5] The Committee of European Insurance and Occupational Pensions Supervisors (CEIOPS), “Catastrophe Task Force report on the Standardised Scenarios for the Catastrophe Risk Module in the Standard Formula,” 2010.

[6] Tokio Marine Holdings. Inc., “Risk Factors,” 1 6 2024. [オンライン]. Available: https://www.tokiomarinehd.com/en/ir/financial/risk.html.

[7] World Climate Research Programme, “WCRP Coupled Model Intercomparison Project

(CMIP)”.

[8] M. Inatsu, T. Suematsu, Y. Tamaki, N. Nakano, K. Mizushima, and M. Shinohara, “Development of pressure-precipitation transmitter,” Journal of Applied Meteorology and Climatology, Vol.58, pp.2453−2468, 2019.

[9] World Meteorological Organizaion, The Atlas of Mortality and Economic Losses from Weather, Climate and Water Extremes (1970−2019), 2021.

[10] T. Loridan, S. Khare, E. Scherer , M. Dixon, and E. Bellone, “Parametric modeling of transitioning cyclone wind fields for risk assessment studies in the Western North Pacific,” J. of Applied Meteorology and Climatology, Vol.54, pp. 624−642, 2015.

[11] AIR Worldwide, “AIR Hurricane Model for the United States,” 2018. [オンライン]. Available: https://www.verisk.com/siteassets/media/downloads/climate/the-air-hurricane-model-for-the-united-states.pdf. [アクセス日: 6 2 2023].

[12] R. E. Tuleya, M. DeMaria, and R. J. R. Kuligowski, “Evaluation of GFDL and simple statistical model rainfall forecasts for U.S. landfalling tropical storms,” Weather and Forecasting, Vol.22, pp. 56-70, 2007.

[13] M. Lonfat, R. Rogers, T. Marchok, and F. Marks, “A parametric model for predicting hurricane rainfall,” Monthly Weather Review, Vol.135, pp. 3086 − 3097, 2007.

[14] J. Grieser and S. Jewson, “The RMS hurricane-rain model,” Meteorologische Zeitschrift,

Vol.21, pp. 79 - 88, 2012.

[15] D. S. Wilks, “Multisite generalization of a daily stochastic precipitation generation model,” Journal of Hydrology, Vol.210, pp. 178-191, 1998.

[16] V. Chow, D. Maidment, and L. Mays, Applied hydrology, New York: McGraw-Hill Book Company, 1988.

[17] S. Coles, An introduction to statistical modeling of extreme values, Springer, 2001.

[18] P. Ailliot, D. Allard, V. Monbet, and P. Naveau, “Stochastic weather generators: an overview of weather type models,” Journal de la société française de statistique, Vol.156, pp. 101-113, 2015.

[19] D. S. Wilks, “Simultaneous stochastic simulation of daily precipitation, temperature and solar radiation at multiple sites in complex terrain,” Agriculture and Forest Meteorology, vol.96, pp. 85-101, 1999.

[20] R. Mizuta, A. Murata, M. Ishii, H. Shiogama, K. Hibino, N. Mori, O. Arakawa, Y. Imada, K. Yoshida, T. Aoyagi, H. Kawase, M. Mori, Y. Okada, T. Shimura, T. Nagatomo, M. Ikeda, H. Endo, M. Nosaka, M. Arai, C. Takahashi, K. Tanaka, T. Takemi, et al., “Over 5,000 years of ensemble future climate simulations by 60-km global and 20-km regional atmospheric models,” Bulletin of the American Meteorological Society, July 2017, 1383-1398, 2017.

[21] M. Ishii and N. Mori, “d4PDF: large-ensemble and high-resolution climate simulations for global warming risk assessment,” Progress in Earth and Planetary Science, Vol.58, 2020.

[22] Y. Tachikawa, K. Miyawaki, T. Tanaka, K. Yorozu, M. Kato, Y. Ichikawa, and S. Kim, “Future change analysis of extreme floods using large ensemble climate simulation data "in Japanese",” Journal of Japan Society of Civil Engineers, Ser B1 (Hydraulic Engineering), Vol.73, pp. 77-90, 2017.

[23] T. J. Yamada, T. Hoshino, and A. Suzuki, “Using a massive high‐resolution ensemble climate data set to examine dynamic and thermodynamic aspects of heavy precipitation change,” Atmospheric Science Letters, Vol.22, e1065, 2021.

[24] T. Tanaka, K. Kobayashi, and Y. Tachikawa, “Simultaneous flood risk analysis and its future change among all the 109 class-A river basins in Japan using a large ensemble climate simulation database d4PDF,” Environmental Research Letters, Vol.16, 2021.

[25] N. Mori, T. Shimura, K. Yoshida, R. Mizuta, Y. Okada, M. Fujita, T. Temur Khujanazarov, and E. Nakakita, “Future changes in extreme storm surges based on mega-ensemble projection using 60-km resolution atmospheric global circulation model,” Coastal Engineering Journal, Vol.61, pp. 295-307, 2019.

[26] N. Mori and T.Shimura, “Tropical cyclone-induced coastal sea level projection and the adaptation to a changing climate,” Coastal Futures , Vol.1, pp. e4, 2023.

[27] K. Sugawara, M. Inatsu, S. Shimoda, K. Murakami, and T. Hirota, “Risk assessment and possible adaptation of potato production in Hokkaido to climate change using a large

number ensemble climate dataset d4PDF,” Scientific Online Letters on the Atmosphere, Vol.17, pp. 24-29, 2021.

[28] K. Murakami, S. Inoue, M. Nemoto, Y. Kominami, M. Inatsu, and T. Hirota, “Projected changes in field workability of agricultural machinery operations for upland crop production with +4 K warming in Hokkaido, Japan,” Journal of Agricultural Meteorology, Vol.78, pp. 155-163, 2022.

[29] S. Kawazoe, M. Inatsu, T. J. Yamada, and T. Hoshino, “Climate change impacts on heavy snowfall in Sapporo with 5-km mesh large ensemble simulations,” Scientific Online Letters on the Atmosphere, Vol.16, pp. 233−239, 2020.

[30] H. Kawase, A. Murata, R. Mizuta, H. Sasaki, M. Nosaka, M. Ishii, and I. Takayabu, “Enhancement of heavy daily snowfall in central Japan due to global warming as projected by large ensemble of regional climate simulations,” Climatic Change, Vol.139, pp. 265−278, 2016.

[31] Y. Kanamori, M. Inatsu, R. Tsurumaki, N. Matsuoka, T. Hoshino, and T. J. Yamada, “Global warming effect and adaptation for a flooding event at Motsukisamu River in Sapporo,” Scientific Online Letters on the Atmosphere, Vol.40, pp. 249−253, 2022.

[32] M. Inatsu, H. Kusaka, and T. Takemi, “The climate change effect,” Impact, Vol.2020, pp. 20-22, 2020.

[33] A. Nishi and H. Kusaka, “Future changes of the extreme high-temperature events influenced by foehn winds in Niigata, Japan,” Atmospheric Science Letters, Vol.24, 2022.

[34] S&P Global Ratings, [オンライン]. Available: https://www.spglobal.com/ratings/en/research/articles/230509-criteria-insurance-request-for-comment-request-for-comment-insurer-risk-based-capital-adequacy-methodolo-12693138. [アクセス日: 9 7 2023].

[35] S. Kravtsov, N. Tilinina, Y. Zyulyaeva, and S. K. Gulev, “Emperical modelling and stochastic simulation of sea level pressure variability,” Journal of Applied Meteorology and Climatology, Vol.55, pp. 1197-1219, 2016.

[36] “Experimental Design of d4PDF,” [オンライン]. Available: https://www.miroc-gcm.jp/d4PDF/design_en.html. [アクセス日: 1 2 2023].

[37] D. Takabatake and M. Inatsu, “Summertime precipitation in Hokkaido and Kyushu, Japan in response to global warming.,” Climate Dynamics, Vol.58, pp.1671−1682., 2021.

[38] M. Kawasaki, Y. Maeda, H. Inomata, S. Akita, S. Kudo, K. Makuuchi, and H. Yamaji, “Technical note on the rate of change in heavy rainfall Intensity for flood control planning to cope with climate change "in Japanese",” National Institute for Land and Infrastructure Management, Ministry of Land, Infrastructure,Transport and Tourism,Japan, 2022.

[39] S. Watanabe, M. Yamada, S. Abe, and M. Hatono, “Bias correction of d4PDF using a

moving window method and their uncertainty analysis in estimation and projection of design rainfall depth,”Hydrological Research Letters, Vol.14, pp. 117-122, 2020.

[40] T. Watanabe, M. Nakamura, Miyuki, N. Utsumi,“The development of bias corrected hourly precipitation dataset for AMeDAS stations based on the projections from d4PDF "in Japanese",”Journal of Japan Society of Civil Engineers, Ser. B1 (Hydraulic Engineering), Vol.74, pp. I_127-I_132, 2018.

[41] Japan Meteorological Agency,“General Information on Climate of Japan.,”[オンライン]. Available: https://www.data.jma.go.jp/gmd/cpd/longfcst/en/tourist.html. [アクセス日: 9 7 2023].

[42] T. Sasai,“dynamical downscaling data for near future atmospheric projection (from Tohoku to Kyushu) by SI-CAT,”Data Integration and Analysis System (DIAS), 2019.

[43] R. Arai, S. Watanabe, Z. Wei, and K. Ikeuchi,“ESTIMATION OF FUTURE FLOOD RISK THROUGHOUT JAPAN USING d4PDF RUNOFF DATA AND SOME ISSUES IN THE METHODd4PDF,” Journal of Japan Society of Civil Engineers Ser B1 (Hydraulic Engineering) 75(2):I_1069-I_1074, 2019.

[44] K. Kobayashi, T. Tanaka, M. Shinohara and Y. Tachikawa,“ANALYZING FUTURE CHANGES OF EXTREME RIVER DISCHARGE IN JAPAN USING d4PDF.,”Journal of Japan Society of Civil Engineers Ser B1 (Hydraulic Engineering) 76(1):140-152, 2020.

[45] T. TANAKA, Y. HIRAMATSU, T. KITANO, and Y. TACHIKAWA, “FUTURE CHANGES OF COOCCURRENCE PROBABILITY OF EXTREME FLOODS USING BIVARIATE EXTREME VALUE THEORY AND d4PDF.,” Journal of Japan Society of Civil Engineers, Ser. B1 (Hydraulic Engineering), 2022, №. 2, p. I_445-I_450, 2022.

[46] S. Watanabe, “Bias Correction for Climate Model Output (1) Method Characteristics and Classification,” J. Japan Soc. Hydrol. and Water Resour.Vol. 33, No.6, 2020.

[47] T. Tanaka, K. Kiyohara, Y. Tachikawa, Comparison of fluvial and pluvial flood risk curves in urban cities derived from a large ensemble climate simulation dataset: A case study in Nagoya, Japan, Journal of Hydrology, Volume 584, article id. 124706., 2020.

[48] Hydrology and Water Resources Research Laboratory, Kyoto University, “1K-FRM/DHM,” 2013. [オンライン]. Available: https://hywr.kuciv.kyoto-u.ac.jp/products/1K-DHM/1K-DHM.html. [アクセス日: 1 4 2024].

[49] Y. Tachikawa and T. Tanaka, Version 2.22, Jun 28, 2018, “User Manual for Distributed Hydrological Model: 1K-DHM-event”.

[50] Uemura, F, Masuya S, Yoshida T, Oomura N, Chiba M, Tomura S, Yamamoto T, Tokioka S, Sasaki H, Hamada Y, et al , “Estimation of annual maximum rainfalls based on a massive ensemble climate predictions in actual river basin.,” J Jpn Soc Civ Eng Ser B1 Hydraul Eng 74(5):115−120. , 2018.

[51] R. Kido, T. Inoue, M. Hatono, and K. Yamanoi , “Assessing the impact of climate change on sediment discharge using a large ensemble rainfall dataset in Pekerebetsu River basin, Hokkaido,” Progress in Earth and Planetary Science volume 10, Article number: 54, 2023.

[52] ISHIDA Junichi, ARANAMI Kohei, KAWANO Kohei, MATSUBAYASHI Kengo, KITAMURA Yuji, MUROI Chiashi, “ASUCA: The JMA Operational Non-hydrostatic Model,” ournal of the Meteorological Society of Japan Ser II 100(5):825-846, 2022.

[53] Water and Disaster Management Bureau, Ministry of Land, Infrastructure, Transport and Tourism, [オンライン]. Available: https://www.mlit.go.jp/river/basic_info/jigyo_keikaku/gaiyou/seibi/. [アクセス日: 16 2024].

[54] H. E. Willoughby, R. W. R. Darling, and M. E. Rahn, “Parametric representation of the primary hurricane vortex. Part II: A new family of sectionally continuous profiles,” Monthly Weather Review, Vol.134, pp. 1102−1120, 2006.

[55] TCFD Consosiam, “TCFD Consortium,” [オンライン]. Available: https://tcfd-consortium.jp/en. [アクセス日: 24 5 2024].

[56] N. Yoshioka, K. Ide, N. Hanasaki, and Y. Hirabayashi, “EVALUATION OF THE REPRODUCIBILITY OF RIVER DISCHARGE WITH DIFFERENT PRECIPITATION DATA IN JAPAN,” Journal of Japan Society of Civil Engineers Ser B1 (Hydraulic

Engineering) 77, 2021.